Thesis for The Degree of Licentiate of Engineering

# Organic cation dynamics in formamidinium and methylbenzylammonium based metal halide perovskites

*A quasielastic neutron scattering investigation*

Kanming Shi

*Department of Chemistry and Chemical Engineering*
Chalmers University of Technology
Gothenburg, Sweden, 2024

**Organic cation dynamics in formamidinium and methylbenzylammonium based metal halide perovskites**
*A quasielastic neutron scattering investigation*

Kanming Shi



Licentiatuppsatser vid Institutionen för kemi och kemiteknik
Chalmers tekniska högskola
Nr 2024:20

Department of Chemistry and Chemical Engineering
Chalmers University of Technology
SE-412 96 Göteborg
Sweden
Phone: +46(0)31 772 1000

Cover:
Schematic illustration of the isotropic reorientational diffusion approximated by the jump diffusion model, where the arrows represent one of the "random" diffusion routes. A detailed introduction to this model can be found on pages 20 - 21.

Printed by Chalmers Digitaltryck
Gothenburg, Sweden 2024.

# Organic cation dynamics in formamidinium and methylbenzylammonium based metal halide perovskites

*A quasielastic neutron scattering investigation*

Kanming Shi

*Department of Chemistry and Chemical Engineering*
*Chalmers University of Technology*

## Abstract

Metal halide perovskites (MHPs) are currently accumulating considerable attention because of their photoluminescent properties and concomitant interest for application in both solar cells and light emitting diodes. However, the underlying physics and chemistry that give rise to these photoluminescent properties remain unclear. In recent years, there has been an increasing body of work indicating that the photoluminescent properties correlate with the dynamics of the organic cations, but the nature of dynamics is also not clear. Accordingly, this thesis focuses on investigations of the organic cation dynamics in a class of promising MHPs, namely the three-dimensional (3D) formamidinium tin halide perovskites $FASnX_3$ [FA = $HC(NH_2)_2^+$, $X$ = Cl, Br] and the vacancy-ordered variant $FA_2SnI_6$, and the zero-dimensional (0D) methylbenzylammonium manganese chloride perovskite $MBAMnCl_3$ (MBA = $C_6H_5CHCH_3NH_3^+$). The main techniques used are quasielastic neutron scattering (QENS) and X-ray diffraction (XRD).

For $FASnX_3$ ($X$ = Cl, Br) and $FA_2SnI_6$, the results unravel the onset of localized rotational dynamics of FA cations present at around 150 K for $FASnBr_3$ and $FA_2SnI_6$, and 250 K for $FASnCl_3$. For all the materials, the dynamics show a strong temperature dependence. For $FASnBr_3$ and $FA_2SnI_6$ at relatively low temperatures ($T \leq$200 K) the dynamics can be generally described as 2-fold and 4-fold jump-diffusion dynamics of the FA cations, whereas at higher temperatures (230–350 K), the dynamics of the FA cations can be considered as isotropic reorientation of the FA cation. The activation energy of the isotropic reorientation is found to be around 66 and 50 meV for $FASnBr_3$ and $FA_2SnI_6$, respectively. The timescale and activation energy of the dynamics of the FA cation vary in the MHPs with different halide ions. A comparison to the QENS data on similar system $FAPbX_3$ ($X$ = Cl, Br, I) indicates a minor effect of the type of metal cation (Pb or Sn), but a stronger effect of the type of halide ion (Cl, Br, I) on the organic cation dynamics.

For the chiral perovskite $MBAMnCl_3$, the results unravel the onset of uniaxial rotational diffusion of the methyl and ammonium, groups at 270 K, and the phenyl group at 300 K. Furthermore, the onset of multiaxial rotational diffusion of the MBA cations are found at 350 K. Additionally, the structure properties of $MBAMnCl_3{\cdot}2H_2O$ have been investigated through XRD. The single crystal XRD studies reveal a hitherto unknown phase of $MBAMnCl_3{\cdot}C_2H_5OH$, but powder XRD results show that the dominant structure in the sample is the $MBAMnCl_3{\cdot}2H_2O$.

It is expected that these new results will be valuable for the development and optimization of design criteria for new MHP materials with desirable properties.

## Keywords

molecular rotational dynamics, quasielastic neutron scattering, X-ray diffraction, metal halide perovskite, photoelectric conversion

$\mathbf{n}^0$


$^{1}H$

# List of Papers

## Appended papers

This thesis is based on the following papers:

[**I**] **K. Shi**, R. Lavén, L. Malavasi, F. Juranyi, and M. Karlsson, *Rotational dynamics of formamidinium cations in $FASnX_3$ (X = Cl, Br) and $FA_2SnI_6$ investigated with quasi-elastic neutron scattering*
*In manuscript.*

[**II**] **K. Shi**, L. Öhrström, W. Cai, J. Qin, F. Gao, and M. Karlsson, *Re-investigation of the crystal structure of the low-dimensional chiral metal halide composite $Hmba_2[Mn_2Cl_6(H_2O)_4]$ by single-crystal X-ray diffraction*
*In manuscript.*

[**III**] **K. Shi**, W. Cai, J. Qin, F. Juranyi, F. Gao, and M. Karlsson, *Rotational Dynamics of Methylbenzylammonium Cations in the Low-Dimensional Chiral Metal Halide Composites $MBAMnCl_3 \cdot 2H_2O$*
*In manuscript.*

# List of Acronyms

| | |
|---|---|
| e.g. | *exempli gratia* (for example) |
| EFWS | Elastic fixed window scan |
| EISF | Elastic incoherent structure factor |
| FA | Formamidinium |
| FWHM | Full width at half maximum |
| HWHM | Half width at half maximum |
| i.e. | *id est* (that is) |
| INS | Inelastic neutron scattering |
| MA | Methylammonium |
| MBA | Methylbenzylammonium |
| MHP | Metal halide perovskite |
| PL | Photoluminescence |
| PSI | Paul Scherrer Institut |
| P-XRD | Powder X-ray diffraction |
| QENS | Quasielastic neutron scattering |
| SC-XRD | Single crystal X-ray diffraction |
| ToF | Time-of-flight |
| VESTA | Visualization for Electronic and Structure Analysis |
| XRD | X-ray diffraction |

# Contents

Chapter 1

# Introduction

The structure and dynamics of materials are vital to understanding how to make predictions and optimizations of new materials and their performance. Materials for optoelectronic conversion, which can convert solar energy and optical signal to electrical energy and electrical signal, play an important role in diverse fields such as energy, communication, display, and lighting.[1] Specifically, photovoltaic cells convert "clean" energy from the sun into electricity for everyday household and industrial use, in parallel, light-emitting devices profoundly affect people's activities and communication through their lighting and display functions.[2] In all these technologies, the conversion efficiency and charge carrier mobility of the materials are crucial properties that impact the performance of the device. In particular, the interactions and coupling among electrons, holes, and phonons within the material significantly influence device performance. Understanding these properties is hence critical for the development of better devices or even new technologies.

Perovskite is a material first discovered in 1839, and it has regained attention in the last decade due to its subclass of metal halide perovskites (MHP), which exhibit outstanding potential in optoelectronic conversion devices.[3,4] The efficiency of a single-junction solar cell based on a MHP has increased by 85% over the past decade.[5] However, the local structure and dynamics of most MHPs are not fully understood.[6] This lack of fundamental understanding hinders the development, integration, and commercialization of devices based on these promising materials.

Neutron scattering can be generally exploited as a powerful technique for studying the local structure and dynamics of materials. In particular, neutron scattering is uniquely suited for studying the dynamics of materials with a characteristic timescale of sub-picoseconds up to several nanoseconds which is arduous with other techniques. The aim of this thesis is to systematically measure, analyze, and understand the local structure and dynamics on this timescale of different organic cations (*e.g.* formamidinium, $CH_5N_2^+$; methylbenzylammonium, $C_8H_{12}N^+$, etc.) in some of the most promising MHPs. The main techniques used for this study are quasielastic neutron scattering (QENS) and X-ray diffraction (XRD).

It is expected that the new fundamental understanding of local structure and dynamics will help the development of design criteria for new and better MHPs, towards their utility in specific applications.

Chapter 2

# Metal halide perovskites

## General characteristics

The word "perovskite" refers to a specific crystal structure first defined by Gustav Rose's discovery of the mineral calcium titanate ($CaTiO_3$) in 1839.* The crystal structure was first described in 1926 from Victor Goldschmidt's work on tolerance factors.[7] However, its structure determination was not achieved until 1945 when the crystal structure of the similar material barium titanate ($BaTiO_3$) was determined with XRD.[8]

Metal halide perovskites (MHPs) refer to perovskite structured materials, similar to $CaTiO_3$ and $BaTiO_3$, but with the oxide ion ($O^{2-}$) substituted for a halide ion (*e.g.* $Cl^-$, $Br^-$, and $I^-$). MHPs show great potential for application in optoelectronic conversion devices.[1,9] Specifically, by benefiting from a suitable and tunable bandgap, strong optical absorption, high defect tolerance, and high free charge carrier density, MHPs show excellent performance in generating, absorbing, and transferring photons and, hence, are promising for application in both solar cells and light-emitting diodes (LEDs).[4] Additionally, they are relatively easy to synthesize.[1,9]

With the increasing amount of research on MHPs over the last decade, the conversion efficiency record of MHP single-junction solar cells increased from 14.1% to 26.7% (Figure 2.1), which is close to the best recorded silicon-based solar cells (27.3%),[5] better than the conventional solar cell (14–19%) and close to the single bandgap efficiency limit of 32.9%.[10] Simultaneously, the photoluminescence (PL) quantum yield † of MHPs such as $MAPbBr_3$ (MA = methylammonium, $CH_3NH_3^+$) can approach 95-100%, which is promising towards application in high-performance MHP LED devices.[11,12] Additionally, due to MHPs generally high absorption/emission efficiency and high defect tolerance, they (*e.g.* $MAPbBr_3$ and $CsPbBr_3$) are promising for applications in lasers.[13–15] Owing to their tunable absorption, MHPs (*e.g.* $MAPbCl_3$ and $MAPbI_3$) have also achieved significant progress in the fields of photodetection in the ultraviolet and infrared regions, respectively.[16–18] Still, the extensive commercial application of MHPs in actual devices continues to encounter

*The name *perovskite* comes after another mineralogist named *Lev Perovski.*

†Quantum yield is the number of photons emitted as a fraction of the number of photons absorbed.

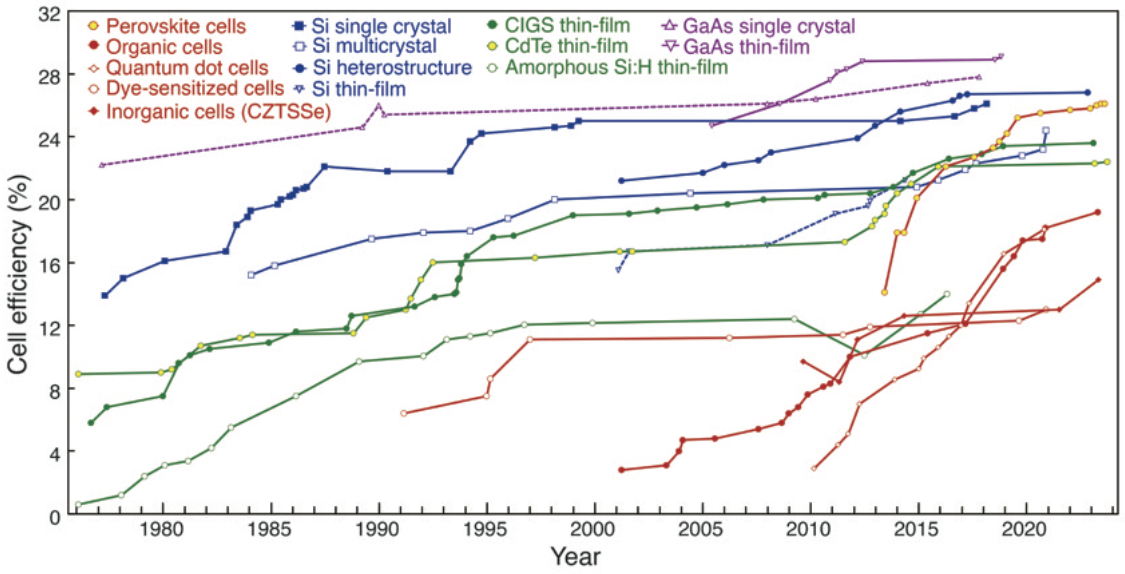


Figure 2.1: Chart of the highest confirmed conversion efficiencies for research single junction cells without solar power concentrator for a range of photovoltaic technologies, plotted from 1976 to 2023.[5] This plot is courtesy of the National Renewable Energy Laboratory, Golden, CO.

barriers because of their limited stability (especially in humid environments), large-scale device performance, and environmental hazard risk.

## 2.1 Structural properties

A typical MHP exhibits the three-dimensional (3D) $ABX_3$ perovskite structure where A is an organic cation (*e.g.* $MA^+$: methylammonium, $FA^+$: formamidinium) or an alkali metal cation (*e.g.* $Cs^+$, $Rb^+$), B is a divalent metal cation (*e.g.* $Pb^{2+}$, $Sn^{2+}$, and $Mn^{2+}$), and X is a halide anion (*e.g.* $Cl^-$, $Br^-$, and $I^-$). Each A-site cation is surrounded by eight $[BX_6]$ octahedra, where each divalent metal ion is located inside of the octahedron, and each anion is shared by 2 octahedra (Figure 2.2). Different modes of $[BX_6]$ octahedron connection may result in structures of lower dimensions. Two-dimensional (2D) MHPs are characterized by that each octahedron shares four vertexes with four other octahedra and expands in a plane (*e.g.* $[CH_3(CH_2)_8NH_3]_2PbI_4$), as shown in Figure 2.3.[19] One-dimensional (1D) MHPs are characterised by that each octahedron shares the vertex with the two closest octahedra shaped as a line structure (*e.g.* $C_4N_2H_{14}PbBr_4$).[20] For Zero-dimensional (0D) MHPs, each octahedron does not connect or share any vertex to any other octahedra (*e.g.* $Cs_4PbI_6$).[21]

Several 3D MHPs have a cubic phase at relatively high temperatures and a tetragonal or orthorhombic phase at lower temperatures. For example, as shown in Figure 2.4, $MAPbI_3$ has an orthorhombic phase below 165 K, a tetragonal phase between 165 and 327 K, and a cubic phase above 327 K.[22] $FAPbI_3$ has a tetragonal phase below 151 K, another tetragonal phase (less distorted from cubic phase) between 151 and 299 K, and a cubic phase above

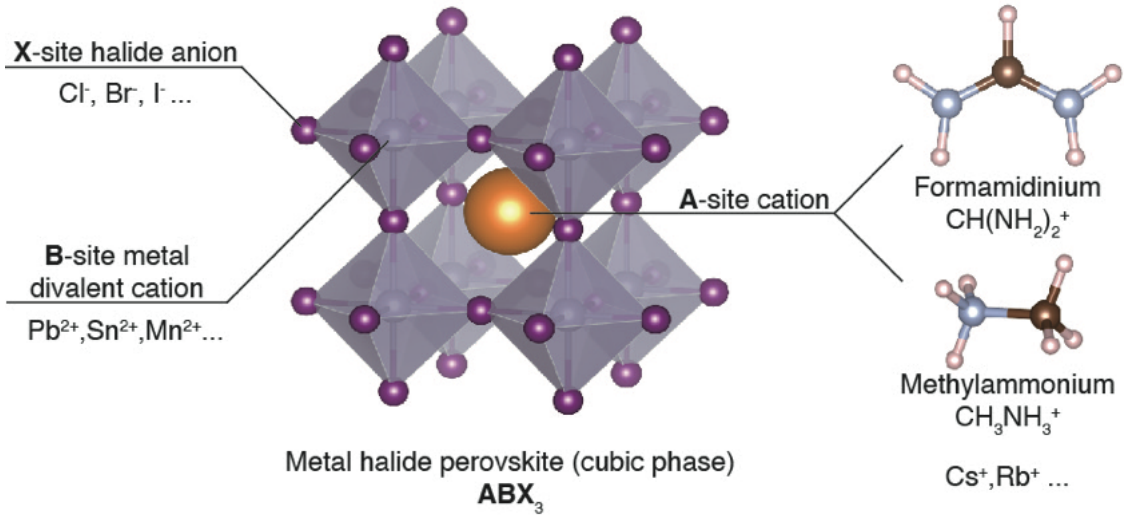


Figure 2.2: Schematic illustration of the cubic $ABX_3$ MHP structure. Color scheme: purple spheres (halide anions), gray spheres (metal cations), orange spheres (A-site cations), brown spheres (carbons), light blue spheres (nitrogens), light pink spheres (hydrogens). Powered by VESTA.

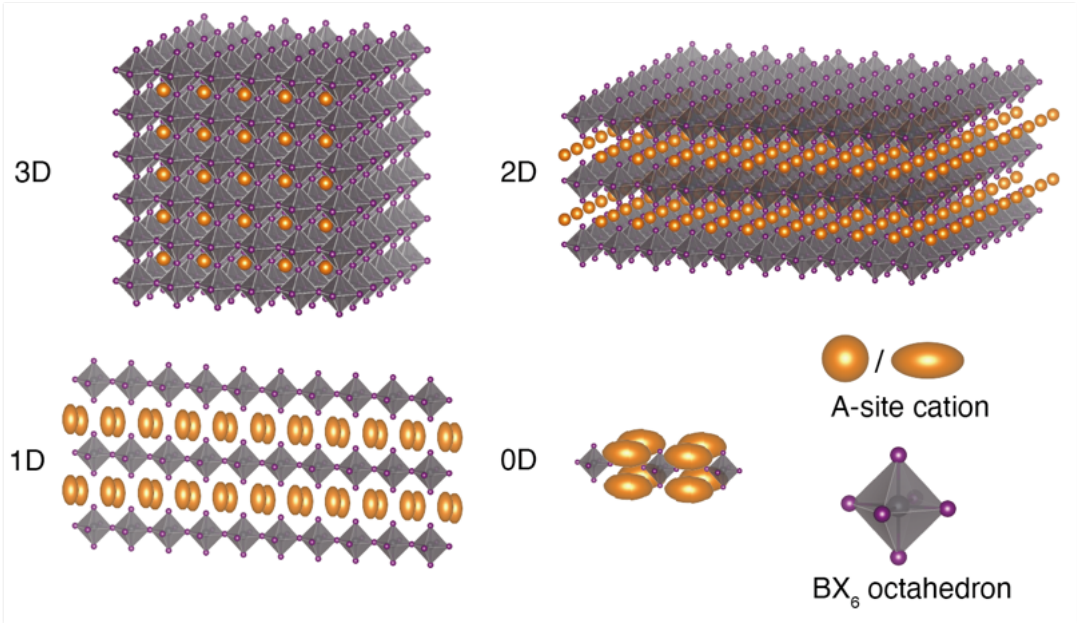


Figure 2.3: Schematic of the various "dimensionality" of MHPs. Color scheme: orange spheres/ellipsoids (A-site cations), gray spheres (B-site metal cations), purple spheres (X-site halide anions). Powered by VESTA.

299 K.[23] These different phase structures are pointed out as having interaction with the organic cation dynamics in the previous study.[24–28]

In the last decade, lower-dimensional MHPs have been proposed as alternatives to their 3D counterparts, because the beneficence of their stable excitons with fast radiative decay can improve the luminescence efficiency of this class of semiconductors. At the same time, the lower dimensional architecture

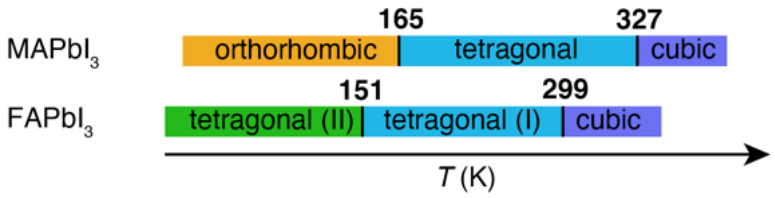


Figure 2.4: Phase transition temperatures diagram of $MAPbI_3$ [22] and $FAPbI_3$ [23].

gives them stability and relaxes geometrical constraints, giving access to a wider range of chemical compositions,[29] and has emerged as promising white phosphors.[30]

In addition to the effects that the octahedral framework has on the structure of MHPs, adjusting the A-site cation can also introduce unique structural and optoelectronic properties. Recently, there has been a growing trend of using chiral organic cations.[‡] Chiral MHPs are becoming attractive to researchers because of their unique characteristics including circular dichroism (CD), and circularly polarized photoluminescence (PL).[31,32] Interestingly, studies have shown that the chirality of the organic cation is transferred to the inorganic sub-lattice, which implies that the luminescence is circularity polarized.[31] By adjusting the sequence of enantiomer (R or S) of chiral organic cation in MHP, the polarization direction of circularly polarized PL can be modulated.[31] Since the first chiral MHP s-methylbenzylammonium (Figure 2.5a) lead bromine ([S-MBA][$PbBr_3$]) was reported,[33] a series of 2D/1D chiral MHPs have been developed. Figure 2.5b shows the crystal structures of the 2D chiral perovskites (R-/S-MBA)$PbI_3$, as well as of the racemic composition (R-MBA)I:(S-MBA)I = 1:1.[31] Though some reports about the dynamics in chiral MHPs have been published,[34,35] very little is known about the dynamics in these materials.

## 2.2 Dynamical properties

As described previously, the structural properties of MHPs profoundly influence their optical characteristics. However, it has been discovered that the dynamics of these materials influence both the structure and optical performance of MHPs.[36–39] Hence, understanding the dynamical properties of MHPs is the key to optimizing them for various technological applications.

The dynamical properties of MHPs may be divided into vibrational dynamics of the inorganic perovskite lattice,[40,41] vibrational and rotational dynamics of the organic cation,[24,42,43] and possibly, but with lower probability, translational dynamics of ions.[44,45]

Of particular concern in this thesis is the organic cation dynamics, which have been invoked to explain several structural and optoelectronic properties of

[‡]Chirality refers to a fundamental structural property that a chiral structure cannot be completely superposable with a mirror image of itself only through rotation and translation, one of a pair of chiral symmetric structures is called an enantiomer which can be differentiated between R and S. R comes from the Latin *rectus* (right), S comes from the Latin *sinister* (left). When the R and S cations account for 50% each, the circularly polarized luminescence characteristics of the material may disappear, and the material is called racemic (rac).

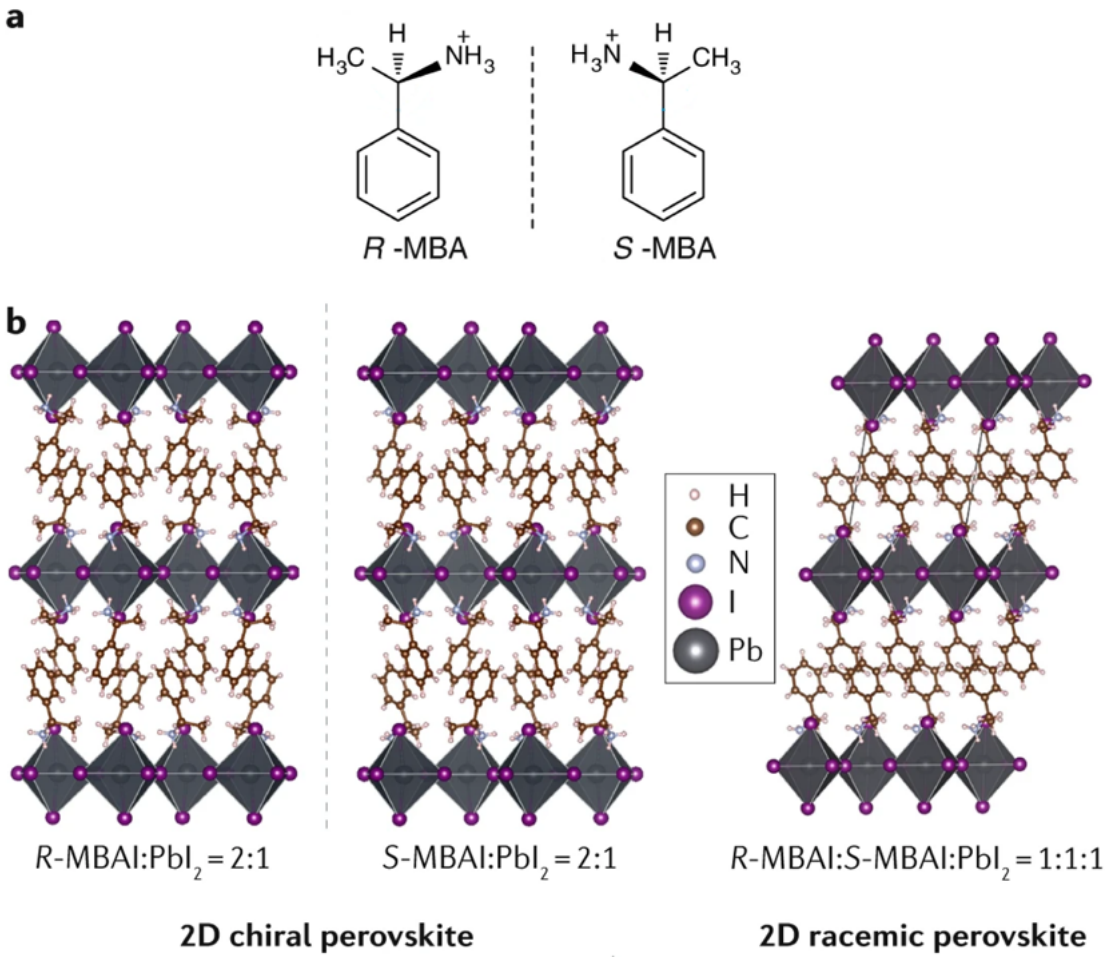


Figure 2.5: Schematic diagrams of **a.** The chiral ligands: MBA (methylbenzylammonium), and **b.** Single-crystal structures of 2D chiral MHPs : R-$MBA_2PbI_4$, S-$MBA_2PbI_4$, and 2D achiral MHP: rac-$MBA_2PbI_4$ with their different precursors ratio (R-/S-MBA)I:$PbI_2$ for synthesis. The dashed lines can be considered as the "mirror" for enantiomers.[31] Used with permission of © Springer Nature BV, from Long, G., Sabatini, R., Saidaminov, M.I. et al. *Chiral-perovskite optoelectronics.* Nat Rev Mater 5, 423–439 (2020); permission conveyed through Copyright Clearance Center, Inc.

MHPs, besides being of great fundamental interest. As an example from 1978, structural studies of $MAPbBr_3$ suggested that at room temperature the [$PbBr_6$] octahedra remain undistorted due to the dynamics of the MA cations.[46] As another example, the rotation of the MA cation has been suggested to lead to the formation of ferroelectric domains, which in turn control the ferroelectric polarization of MHPs.[25,47] Subsequent research revealed that the reorientation of the organic cations affects the tilting of the perovskite octahedra, which can break and help in the formation of hydrogen bonds between the organic cation and the octahedra, and this is considered one of the reasons for phase separation in MHPs.[48] Lately, there also have been several studies suggesting that the reorientational dynamics of cations are one of the causes of charge screening, with consequent stabilization of photogenerated charge carriers and

prevention of fast charge recombination.[36,49]

In recent years, dynamical properties of organic cations have been investigated through QENS,[24–27,50–60] nuclear magnetic resonance (NMR),[61–63] and infrared (IR) spectroscopy.[64,65] Meanwhile, a lot of computational work by molecular dynamics (MD) simulations has been also performed.[66–68] These experiments and simulations have characterized the timescale, geometry, and activation energy of the dynamics of organic cations in various MHPs, and in some cases explored their correlation with properties such as antiferroelectric or ferroelectric behaviour,[25] crystal structure,[38] stability,[39] and photovoltaic hysteresis.[69] Most studies have focused on MAPb$X_3$ ($X$ = Cl, Br, and I) and FAPb$X_3$ ($X$ = Cl, Br, and I). These results show that the dynamics of the organic cations can be generally explained as localized "jump-diffusion"[§] dynamics over a specific number of sites which depends on the symmetry of the organic cation as well as the symmetry of the surrounding inorganic MHP framework.

Table 2.1 shows a summary of key dynamical properties for $MAPbI_3$ and $FAPbI_3$, as obtained from previous studies. As can be seen, the localized dynamics of MA and FA cations occur on the timescale of picoseconds. For $MAPbI_3$, the dynamics evolve from 3-fold ($C_3$) jump-diffusion of methyl and ammonium around the C–N axis, in the low-temperature ($T<$ 165 K) orthorhombic phase, to $C_3$ jump diffusion coupling with 4-fold ($C_4$) jump diffusion around the C–N axis in the intermediate-temperature (165 K $<T<$ 327 K) tetragonal phase and high-temperature ($T>$ 327 K) cubic phase (Figure 2.6).[24] For $FAPbI_3$, the dynamics evolve from $C_4$ jump diffusion around the N–N axis in the low-temperature ($T<$ 285 K) tetragonal phase to isotropic reorientational diffusion[28] or tri-axis (N–N axis, C–H axis, and the vertical axis) rotational diffusion[70] in the high-temperature ($T>$ 285 K) cubic phase (Figure 2.6). Besides $MAPbI_3$ and $FAPbI_3$, the organic cations dynamics in the halogen-substituted materials $MAPbBr_3$,[51,52] $MAPbCl_3$,[55,56] and $FAPbBr_3$,[26,27,50] have been also investigated using QENS. The results of these studies show that the MA and FA cation dynamics are affected by the type of X-site cation, but the main types of jump-diffusion mechanisms persist. Furthermore, mixed-cation systems, such as $FA_xMA_{1-x}PbI_3$,[26,60] and $MAPbI_{2.94}Cl_{0.06}$,[55] have been investigated. In general, the A-site organic cation dynamics in these MHPs with different X-site ions show similar geometry in the same phase with a variance in the timescale and the activation energy of the dynamics.

Compared to 3D MHPs, fewer QENS studies have focused on investigations of the organic cation dynamics in lower dimensional MHPs. These studies are limited to QENS studies of the 2D MHP $(OA)_2PbI_4$ (OA = octylammonium), and $A_2PbBr_4$ [$A$ = n-butylammonium (nBA), 1,8-diaminooctammonium (ODA), and 4-aminobutyric acid (GABA)]. Figure 2.7 shows that the organic cation octylammonium has 2-fold ($C_2$) rotation of the head group $NH_3$–$CH_2$, $C_3$ rotation of the terminal -$CH_3$ and -$NH_3$ groups, and librations of the -$CH_2$- group at different temperatures.[71] Figure 2.8 shows that the organic cation

[§]Jump diffusion refers to an atom "jumping" from one site to another. The time for a jump is considered to be negligible. The time between two consecutive jumps is called the residence time.

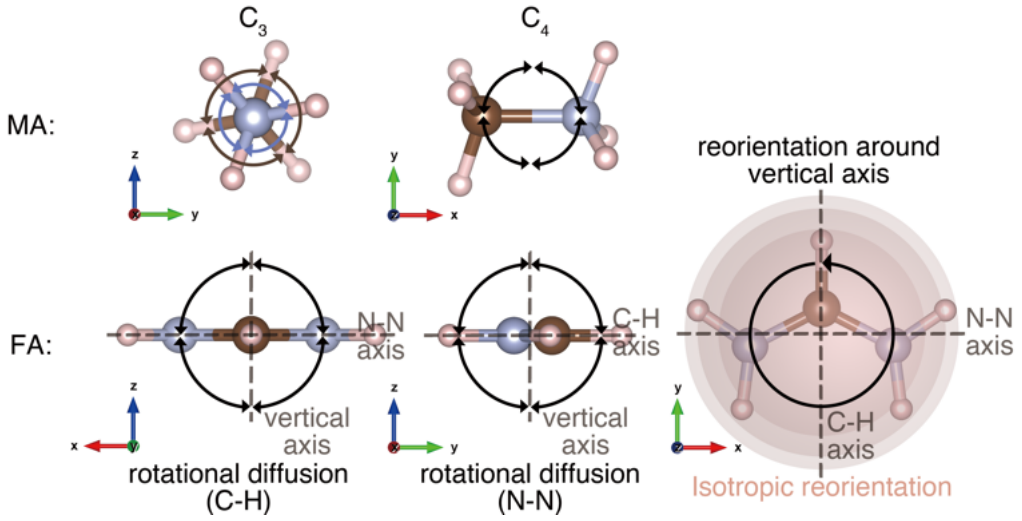


Figure 2.6: Schematic illustration of localized dynamics of MA and FA cations in $A\mathrm{Pb}X_3$ ($A$ = MA, FA; $X$ = Cl, Br, and I).

Table 2.1: Compilation of dynamics data for MA and FA dynamics in $MAPbI_3$ and $FAPbI_3$, respectively.

| | Method | $C_3$ $(\tau, T)$ | $C_4$ $(\tau, T)$ | Reference No. |
|---|---|---|---|---|
| $MAPbI_3$ (tetragonal) | QENS | 0.82 ps 300 K | 4.70 ps 300 K | 24 |
| | NMR ($^2$H, $^{14}$N) | 0.576 ps 300 K | 1.73 ps 300 K | 62 |
| | NMR ($^2$H, $^{14}$N) | 0.15 ps 298 K | 1.95 ps 298 K | 70 |
| | 2D IR | | 3 ps room temperature | 64 |
| | 2D IR | | 3 ps room temperature | 65 |
| | Method | rotational diffusion $(\tau, T)$ | | Reference No. |
| $FAPbI_3$ (cubic) | QENS | 64 - 9.4 ps $C_4$ N-N axis 140 - 285 K (tetragonal) | 1.5 ps Isotropic 350 K | 28 |
| | NMR ($^2$H, $^{14}$N) | | 8.7 ps Isotropic 294 K | 63 |
| | NMR ($^2$H, $^{14}$N) | 0.38 ps N-N axis 1.05 ps C-H axis 1.3 ps vertical axis 298 K | | 70 |

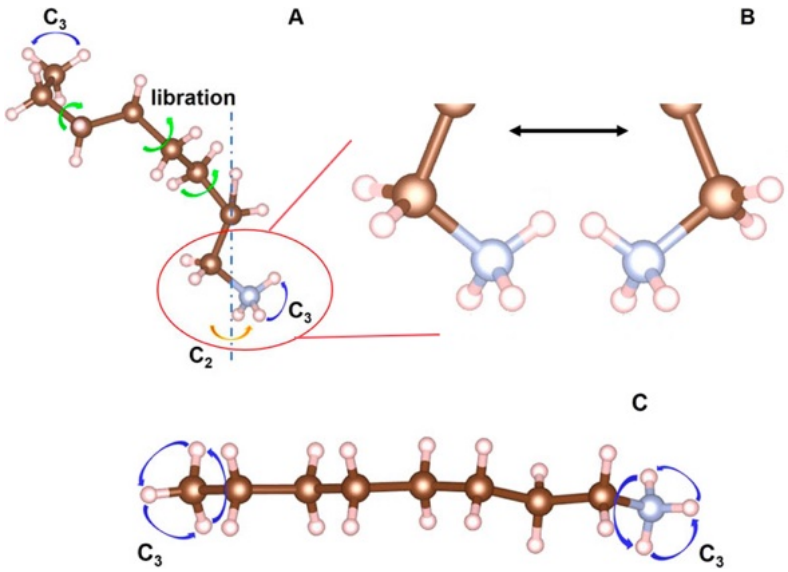


Figure 2.7: Rotational diffusion modes of the OA cation in different phases of $(OA)_2PbI_4$ including (A), (B): high-temperature orthorhombic phase: $C_3$ of $-CH_3$, $C_2 \otimes C_3$ of $-NH_3$, $C_2$ of the adjacent $-CH_2-$, and slow librations of other $-CH_2-$ groups. And (C): intermediate and low-temperature monoclinic phases: $C_3$ of $-CH_3$ and $-NH_3$.[71] Used with permission of © American Institute of Physics, from Hu, Xiao; Zhang, Depei et al. *Crystal structures and rotational dynamics of a two-dimensional metal halide perovskite $(OA)_2PbI_4$.* Chem. Phys. 7 January 2020; 152 (1): 014703; permission conveyed through Copyright Clearance Center, Inc.

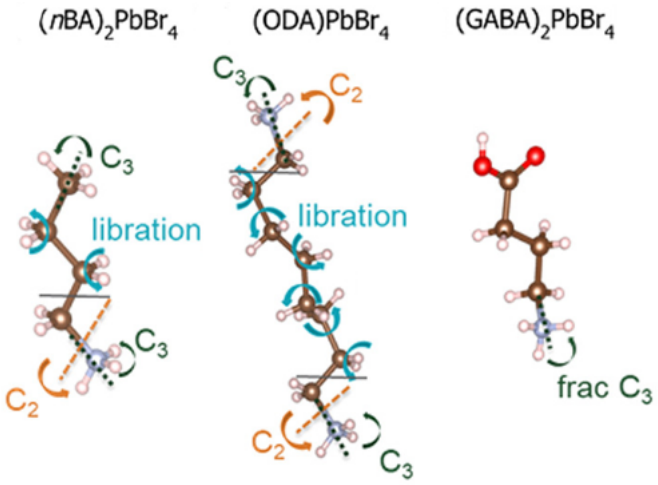


Figure 2.8: Rotational diffusion modes of the cations in $A_2PbBr_4$ ($A$ = nBA, ODA, and GABA).[57] Copyright © 2022 American Chemical Society, CC BY, from Alexandra A. Koegel, James R. Neilson, et. al.

nBA and ODA exhibits $C_2$ rotation of the head group $NH_3$–$CH_2$, $C_3$ rotation of the terminal $-CH_3$ and $-NH_3$ groups, and librations of the $-CH_2-$ group. The organic cation GABA only has $C_3$ rotation of the partial $-NH_3$ group.[57] It has also been reported that the larger A-site cation dynamics radii could lead to

less broadband luminescence by reducing the octahedral out-of-plane tilt angle in layered halide perovskites.[57]

## 2.3 Metal halide perovskites studied in this thesis

The work in this thesis has focused on studies of two classes of MHPs, including the 3D formamidinium [FA = $HC(NH_2)_2^+$] tin halide perovskite ($FASnX_3$, $X$ = Cl, Br) and $FA_2SnI_6$, and the methylbenzylammonium (MBA = $C_6H_5CHCH_3NH_3$) manganese halide chiral perovskite [$(MBA)MnCl_3{\cdot}2H_2O$].

### 2.3.1 $FASnX_3$ ($X$=Cl, Br) and $FA_2SnI_6$

Although Pb-based MHPs such as $FAPbI_3$ and $MAPbI_3$ show promising photoelectric conversion performance, regrettably, Pb is toxic which brings potential hazard risk to the environment. Therefore, much research is currently focused on the investigation of Pb-free MHPs.[72–75] In this context, Sn-based MHPs are considered to be one of the most attractive substitutions of Pb-based MHPs.[76]¶ With the suitable ionic radius of $Sn^{2+}$ and bandgap for optoelectronic applications, Sn-based MHPs are considered as a new way for lead-free MHPs.[77] Similarly to $FAPbI_3$, $FASnI_3$ undergoes temperature-dependent phase changes. More specifically, $FASnI_3$ exhibits a cubic $\alpha$ phase (space group $Pm\bar{3}m$) at above 275 K, a tetragonal $\beta$ phase (space group $P4/mbm$) at 150 - 250 K, and an orthorhombic $\gamma$ phase (space group $Pnma$) at below 125 K (Figure 2.9).[78] As it may have been noticed, there are temperature gaps between different phases because $FASnI_3$ shows a second-order phase transition with mixed phases.[78] $FA_2SnI_6$ is a vacancy-ordered metal halide double perovskite‖

¶It is worth pointing out that the acidic degradation subproducts and oxidation of the $Sn^{2+}$ are also considered as potential hazard risks.[76]

‖Double perovskites refer to a perovskite [$A_2B(II)B'(II)X_6$ or $A_2B(IV)X_6$] with a long-range ordered unit cell whose size is doubling the $AB(II)X_3$ perovskite.

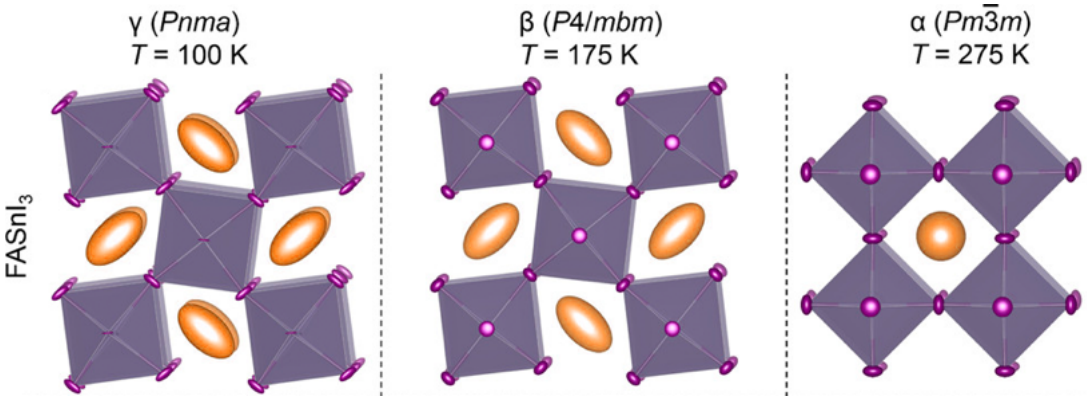


Figure 2.9: Structural evolution of $FASnI_3$ with temperature. Atomic displacement parameters are shown as 50% probability ellipsoids. Colour scheme: orange spheres (FA), purple spheres (I).[78] Copyright © American Chemical Society, CC BY, from Emily C. Schueller, Geneva Laurita, et. al.

(Figure 2.10).[79] However, the dynamical properties of these materials, especially regarding the FA cation dynamics, are still unknown. Here, I have focused on the investigations of the following unsolved research questions:

- What is the nature of localized diffusional dynamics of FA in FASn$X_3$ ($X$ = Cl, Br) and $FA_2SnI_6$, such as the geometry, timescale, and activation energy of the dynamics?
- How do the localized dynamics of FA cations change with temperature in FASn$X_3$ ($X$=Cl, Br) and $FA_2SnI_6$?
- What is the difference in FA cation dynamics between FASn$X_3$ ($X$=Cl, Br) and $FA_2SnI_6$?
- How does the FA cation dynamics compare with the FA cation dynamics in prototypical FAPb$X_3$ ($X$=Cl, Br, I)?

### 2.3.2 R-/S-MBAMnCl$_3$·2H$_2$O

R-/S-MBAMnCl$_3$·2H$_2$O represents a novel chiral 0D MHP, that was first reported in 2022 and that exhibits white light emission upon excitation at 330 nm.[80] Structurally, R/S-MBAMnCl$_3$·2H$_2$O exhibits a monoclinic structure of the $P_{21}$ group, with the lattice parameters of a = 6(2) Å, b = 36.409 Å, and c = 6.377 Å.[80] It may be described as a 0D structure where two Mn-Cl octahedra, with two of the $Cl^-$ replaced by $H_2O$ molecules, bridge by two of these $H_2O$ molecules. This is then surrounded by large hydrogen-bonded MBA cations (Figure 2.11). These structural results were obtained from single crystal XRD (SC-XRD) on a single crystal sample at 100 K, however, with an unneglectable, and crystallographically unacceptable large uncertainty in the lattice parameter a = 6(2) Å.[80] For this purpose, I have re-investigated the crystal structure of R/S-MBAMnCl$_3$·2H$_2$O, using SC-XRD, with the aim of a more accurate description of the crystal structure. In addition, I have investigated the nature of organic cation dynamics in R/S-MBAMnCl$_3$·2H$_2$O by using QENS, with the following main questions being targeted:

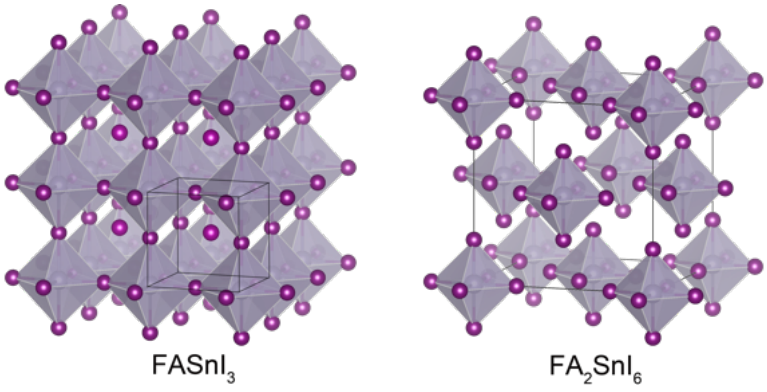


Figure 2.10: Schematic illustration of the inorganic framework of the cubic phase of $FASnI_3$ and $FA_2SnI_6$. The black lines refer to the unit cell. Colour scheme: purple spheres (I), grey spheres (Sn).[78,79]

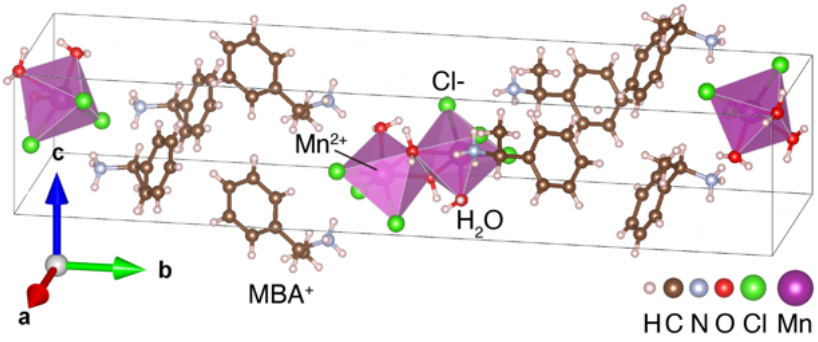


Figure 2.11: Schematic illustration of the $MBAMnCl_3{\cdot}2H_2O$ structure, with the unit cell indicated.

- Is it possible to obtain a more accurate description of the crystal structure of $MBAMnCl_3{\cdot}2H_2O$ on the basis of SC-XRD measurements?
- Is there any different phase of $MBAMnCl_3{\cdot}2H_2O$? If so, which is the main phase in the sample?
- What are the nature of the localized dynamics of the chiral organic cation R-MBA and S-MBA in R-/S-$MBAMnCl_3{\cdot}2H_2O$ including its geometry, timescale, and activation energy of the dynamics? How do the dynamics correlate to the investigated temperature and the type of enantiomer?
- What is the correlations to organic cation dynamics in $FASnX_3$ ($X$ = Cl, Br), $FA_2SnI_6$?

Chapter 3

# Methodology

This chapter begins with a short historical account of the discovery and basic properties of the neutron and then gives the theoretical background needed to understand the key characteristics of the main experimental techniques used in this thesis, *i.e.* quasielastic neutron scattering and X-ray diffraction.

## 3.1 Neutron scattering

### 3.1.1 The basic properties of neutrons

The concept of the neutron was built by Ernest Rutherford in 1920, named by William Harkins in 1921, and the evidence of its existence was found by James Chadwick in 1931.[81–83] The neutron is a subatomic particle, whose mass is close to the proton and much larger than the electron,[84] has the third longest mean lifetime among the subatomic particles (bosons not included) after the proton and electron.[85] Compared to the proton and electron, a neutron is composed of one up quark, two down quarks, and gluons, which leads to its electrical neutrality. Still, the distribution of quarks with spin angular momentum $\pm 1/2\ \hbar$ makes the neutron possess a weak magnetic moment.[86*] With a relatively long lifetime, electrical neutrality, and weak magnetic moment, neutron scattering techniques can be used to investigate both the dynamics and structure of a material. The probed length scale and energy scale are closely related to the wavelength and energy of the neutron. Table 3.1 shows a classification of neutrons according to their energy and wavelength. In this thesis, cold neutrons (0.05 meV $<E<$ 14 meV) have been used.

### 3.1.2 Scattering theory

Figure 3.1 shows the general geometry of a neutron scattering process, in which an incident neutron with wavevector $\boldsymbol{k}_\mathrm{i}$ and kinetic energy $E_\mathrm{i}$ is scattered on a sample. The neutron is scattered to a solid angle $\mathrm{d}\Omega$ with scattering angle $\theta$ and azimuthal angle $\Phi$, and the wavevector and kinetic energy of the scattered neutron are $\boldsymbol{k}_\mathrm{f}$ and $E_\mathrm{f}$.

*Magnetic neutron scattering is not relevant to my work, hence the description of the scattering theory is focused on nuclear neutron scattering.

Table 3.1: Classification of neutrons according to their energy range and wavelength range.

| **Classification** | **Energy** | **Wavelength** |
|---|---|---|
| Ultra cold neutron | $\leq$ 0.05 meV | 40 Å $\leq$ |
| Cold neutron | 0.05 meV - 14 meV | 2.4 - 40 Å |
| Thermal neutron | 14 meV - 200 meV | 0.6 - 2.4 Å |
| Hot neutron | 200 meV - 1 eV | 0.3 - 0.6 Å |
| Epithermal neutron | 1 eV $\leq$ | $\leq$ 0.3 Å |

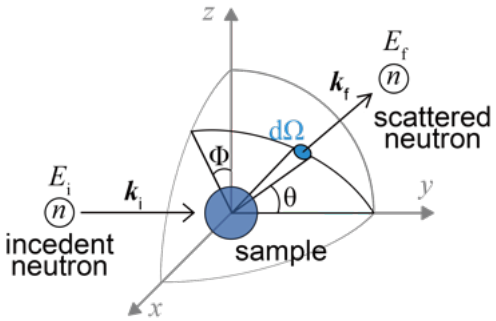


Figure 3.1: Schematic illustration of the scattering geometry. The incident neutrons with wavevector $\boldsymbol{k}_\mathrm{i}$ and kinetic energy $E_\mathrm{i}$ scatter on the sample with the scattering angle $\theta$ and azumital angle $\phi$. The neutrons with wavevector $\boldsymbol{k}_\mathrm{f}$ and kinetic energy $E_\mathrm{f}$ are scattered into the solid angle element $\mathrm{d}\Omega$.

One of the most crucial aspects of a material subjected to neutron scattering is its ability to scatter, transmit, and absorb neutrons. Except for the absorption, these abilities may be described by the neutron scattering cross-section $\sigma$ which describes the ratio of scattered neutron rate to the incident neutron flux $\Psi$ [87]:

$$\sigma = \frac{n_{\mathrm{scatterd/sec.}}}{\Psi} \tag{3.1}$$

$$\frac{d\sigma}{d\Omega} = \frac{1}{\Psi}\frac{n_{\mathrm{d}\Omega\mathrm{/sec.}}}{d\Omega} \tag{3.2}$$

The magnitude of the scattering strength depends on the nuclei, which varies with the isotope and can be described by its scattering length $b$ (more detailed definition and derivation can be found in Appendix B.1):

$$\frac{d\sigma}{d\Omega} = b^2 \tag{3.3}$$

During the scattering, the exchange of momentum is defined as:

$$p = \hbar(\boldsymbol{k}_i - \boldsymbol{k}_f) = \hbar\mathbf{Q} \tag{3.4}$$

where $\mathbf{Q}$ is the change of neutron wavevector, and the exchange of energy:

$$E = E_\mathrm{i} - E_\mathrm{f} = \hbar\omega \tag{3.5}$$

where $\omega$ represents the change in the neutron wave's angular velocity.

Due to the consideration of energy variation, energy dependence needs to be accounted for in the scattering equations. This is done in the double differential cross section which is proportional to the number of neutrons scattered per time unit into a small solid angle with final energy from $E_f$ to $E_f + dE_f$:

$$\frac{d^2\sigma}{d\Omega dE_f} = \frac{1}{\Psi} \frac{n_{\mathrm{d}\Omega/\mathrm{sec.}} \in [E_f; E_f + dE_f]}{d\Omega dE_f} \tag{3.6}$$

The structure factor $S(Q, E)$, as a more experimental index that focuses on the $\mathbf{Q}$ and $E$ from the sample but not the incident or scattered neutron can be adapted from the double differential cross-section:

$$\frac{d^2\sigma}{d\Omega dE_f} = \frac{\sigma}{4\pi} \frac{k_f}{k_i} S(\mathbf{Q}, E) \tag{3.7}$$

By taking the Fourier transform of $S(Q, E)$ one can obtain the time-related intermediate function $I(\mathbf{Q}, t)$, and the Van Hove correlation function $G(\mathbf{R}, t)$, respectively. The space-time correlation function $G(\mathbf{R}, t)$ describes the probability that a particle can be found at position $\mathbf{R}$ at time $t$.

$$S(\mathbf{Q}, E) \overset{FT}{\rightleftharpoons} I(\mathbf{Q}, t) \overset{FT}{\rightleftharpoons} G(\mathbf{R}, t) \tag{3.8}$$

Therefore, the relation between the neutron scattering process and the space-time information of atoms in the material can be found, and the dynamical properties of the atoms can be further analyzed. For a much more detailed definition and derivation of the double differential cross section and correlation functions, the reader is referred to Appendix B.2.

### 3.1.3 Coherent and incoherent scattering

Nuclear neutron scattering involves both coherent and incoherent parts. Coherent scattering involves correlations between the position of a nucleus j at the initial time and the position of the other nucleus j' at a later time. Therefore, it describes the interference effect of waves produced by neutrons interacting with all the nuclei in the sample. It provides information about the collective motions and correlations among different nuclei, such as phonons or structural arrangements in a material. Incoherent scattering, on the other hand, involves correlations between the position of the same nucleus j at an initial time and its position at a later time $t$. In incoherent scattering, the scattered waves from different nuclei do not interfere with each other. In dynamics studies, incoherent scattering reflects the motion of individual atoms or molecules rather than collective motions. The strength of the coherent and incoherent scattering depends on the coherent and incoherent cross-section of the isotopes in the sample. As shown in Figure 3.2, $^1$H has a very large total scattering cross-section (mainly contributed by the incoherent cross-section) which shows4 that neutron scattering is often a very powerful technique for the study of single-particle self-dynamics of hydrogen in many materials. The detailed derivation of the coherent and incoherent cross section can be found in Appendix B.2

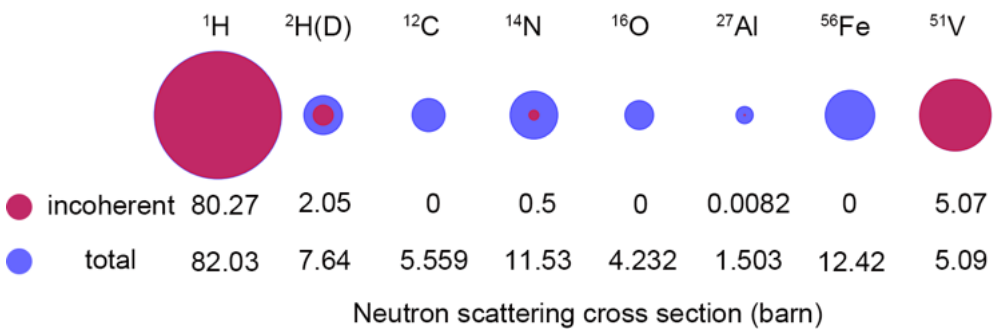


Figure 3.2: Schematic illustration and data of the incoherent and total cross section for different nuclei (1 barn = $1 \cdot 10^{-28}$ m$^2$).

### 3.1.4 Incoherent quasielastic neutron scattering

Figure 3.3 shows a general neutron scattering spectrum, plotted as scattering intensity versus energy transfer (at a specific **Q** value). The spectrum may be divided into three parts: elastic scattering, quasielastic scattering, and inelastic scattering. Elastic scattering refers to scattering with no energy transfer between the neutron and the nuclei. Quasielastic neutron scattering refers to scattering with a slight energy transfer between the neutron and the nuclei. It is featured by a broadening of the elastic peak usually coming from atomic diffusion. Inelastic scattering is featured by an energy transfer between the neutron and nucleus and which is manifested as peaks at $\Delta E \neq 0$.

While quasielastic and inelastic scattering can be coherent in nature, this thesis focuses on studies of hydrogen dynamics in material. Since hydrogen scatters mainly incoherently (see Figure 3.2), the quasielastic signal can be approximated as incoherent [$S(\mathbf{Q}, E) \approx S_{\text{inc}}(\mathbf{Q}, E)$, $I(\mathbf{Q},t) \approx I_{\text{inc}}(\mathbf{Q},t)$]. The correlation function $G(\mathbf{R},t)$ for the incoherent scattering can be used to describe the probability of an atom itself can be found at position **R** marked as $G_{\text{s}}(\mathbf{R},t)$.

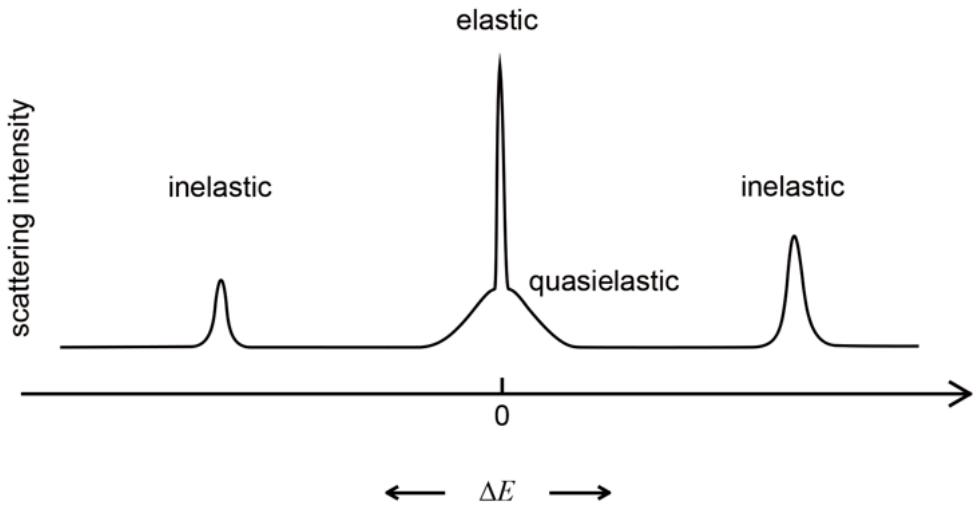


Figure 3.3: Schematic of elastic, quasielastic, and inelastic scattering peaks in $S(E)$.

The links among these three correlation functions through the reversible Fourier transform are the key to investigating the atomic self-diffusional dynamics through quasielastic neutron scattering:

$$S_{\mathrm{inc}}(\mathbf{Q},E) \overset{FT}{\rightleftharpoons} I_{\mathrm{inc}}(\mathbf{Q},t) \overset{FT}{\rightleftharpoons} G_{\mathrm{s}}(\mathbf{R},t) \tag{3.9}$$

#### 3.1.4.1 Analysis of QENS data

In the analysis of QENS data, the neutron scattering spectrum is normally approximated with a function of the form:

$$S_{\mathrm{inc}}(Q,E) \propto A_{i=0}(Q)\delta(E) + \sum_{i\neq 0} A_i(Q)\mathcal{L}_i(Q,E) \tag{3.10}$$

Here, the first term $A_{i=0}(Q)\delta(E)$ describes the elastic scattering. The second term is a series of Lorentzian functions $\mathcal{L}(Q,E)$:

$$\mathcal{L}(Q,E) = \frac{1}{\pi}\frac{\gamma(Q)}{E^2+[\gamma(Q)]^2} \tag{3.11}$$

with half-width-at-half-maximum (HWHM) $\gamma$, which describes the quasielastic scattering. The $0 \leq A_i(Q) \leq 1$ are the normalized $Q$ dependent amplitude of structure factors ($\sum_i A_i(Q) = 1$). The $\gamma$ has a reciprocal relation to the correlation time $\tau$ ($\gamma = \hbar/\tau$), and $\gamma/\hbar$ can describe the diffusion rate of the diffusing atom from one position to the other correlated positions.

The QENS can arise from long-range translational diffusion and/or localized diffusion of atoms. Long-range translational diffusion, which refers to the probability of the mobile species returning to the initial position approaches zero after a relatively long time $[G_s(\mathbf{R}(t=0), t\rightarrow+\infty) = 0]$, is commonly observed in liquid samples and ionic conductors. For long-range diffusion, the correlation time $\tau(Q)$ follows Brownian translational diffusion and the incoherent scattering function can be found at a limited $Q$-value which can be described by Einstein's random walk theory[87]:

$$S_{\mathrm{inc}}(Q,\hbar\omega) = \frac{1}{\pi}\frac{DQ^2}{\omega^2+(DQ^2)^2} \tag{3.12}$$

$$\tag{3.13}$$

where $D$ is the diffusion coefficient, and $\tau(Q)^{-1} = DQ^2$ when $\gamma(Q) = \hbar/\tau(Q) = \hbar DQ^2$.

Localized diffusion refers to the probability of the mobile species to return to the initial position approaches a constant c ($0 < \mathrm{c} < 1$) after a relatively long time $[G_s(\mathbf{R}(t=0), t\rightarrow+\infty) = \mathrm{c}]$. For localized diffusion, two important conclusions can be found:
1. The HWHM $\gamma(Q)$ of Lorentzian is $Q$ independent, which can be understood by the probability, that the nuclei can be found at position $R$ at a long enough time, is independent of the initial position;
2. The amplitude $A_0$ of elastic scattering is zero in long-range diffusion, which

can be obtained from the Fourier transform $G_s(\mathbf{R}, t \to +\infty) = 0 \overset{FT}{\Rightarrow} I_{\text{inc}}(\mathbf{R}, t \to +\infty) = 0 \overset{FT}{\Rightarrow} A_0 = 0$.

These statements can help to distinguish the long-range and localized diffusional dynamics from the experimental data. For the localized diffusion, the correlation time ($\tau$) from the dynamics giving rise to QENS can be derived from:

$$\tau = \hbar/\gamma \tag{3.14}$$

In a limited temperature range ($T_0 \leq T \leq T_1$) with a relatively ideally tiny change of the external influence (*e.g.* the same crystal phase), the molecular dynamical activation energy $E_a$ often can be found by following the Arrhenius equation through the fitting of temperature-dependent $\tau$ results:

$$\tau(T) = \tau(T_0) \cdot e^{-E_a/[k_{\text{B}}(T-T_0)]} \tag{3.15}$$

where $k_{\text{B}}$ is the Boltzmann constant.

As described before, the localized diffusion will bring a fixed probability that a self diffused nuclei can be found within a bounded space, $[G_s(\mathbf{R}_{t=0}, t \to +\infty) \to c]$, where the relative intensity of this elastic component is known as the elastic incoherent structural factor (EISF=$\text{A}_0$) (the derivation process can be obtained in Appendix B.4). EISF can be experimentally calculated by the ratio of the area of the elastic peak to the area of the elastic peak plus quasielastic peak(s) *i.e.*:

$$\text{EISF} = \frac{\text{Area}_{\text{elastic}}}{\text{Area}_{\text{elastic}} + \text{Area}_{\text{quasielastic}}} \tag{3.16}$$

The EISF contains information about the geometry of localized dynamics. As shown in Figure 3.4, it decays from 1 at $Q = 0$, and varies by the spatial information of the atom including the number of residence positions $N$ and the distances $d$ among the positions ($d = |\mathbf{R}_{\text{i}} - \mathbf{R}_{\text{j}}|$). In the simple equivalent site (equal mean residence time) jump-diffusion cases, the EISF is approaching the reciprocal of the number of residence positions at larger $Q$, and the $Q$ position of the lowest value of EISF is proportional to the reciprocal of the jump distance. The information about geometry contained by EISF needs to be extracted by a suitable diffusion model which can fit the EISF and also follows the laws of physics and chemistry.

Figure 3.5 shows several common diffusion models, including the 2-site jump-diffusion model which considers the particle jump between 2 sites with mean residence times $\tau_1$ and $\tau_2$ and jump distance $d = |\mathbf{R}_1 - \mathbf{R}_2|$ (Figure 3.5(a).[87] The N-fold jump-diffusion model which is supposed that the particle can only directly jump to the nearest 2 sites on the circle, for instance in Figure 3.5(b), when the particle is on the site $\mathbf{R}_i$ the next jump of it can only jump to $\mathbf{R}_{i-1}$ or $\mathbf{R}_{i+1}$. In other words, $\tau_{i,j}^{-1} = 0$ when $|i - j|>1$. The isotropic reorientation model is similar to the underlying logic of the previous model, where an equivalent site model is also considered, but considering the spatial angle instead of the plane angle (Figure 3.5(c)).

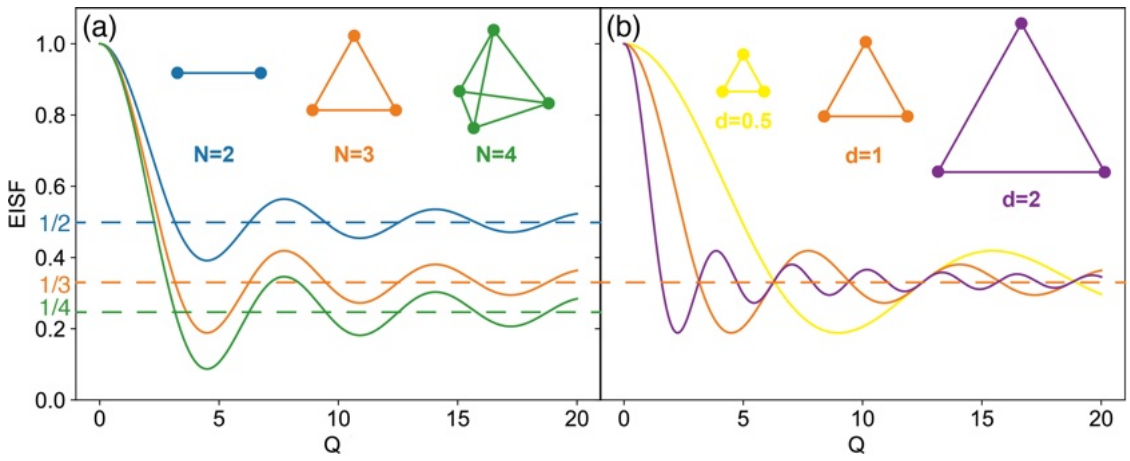


Figure 3.4: EISF for the jump diffusion over N equivalent sites with (a) $d = 1$ and for different $N$ for values, and (b) $N = 3$ with different $d$ values.

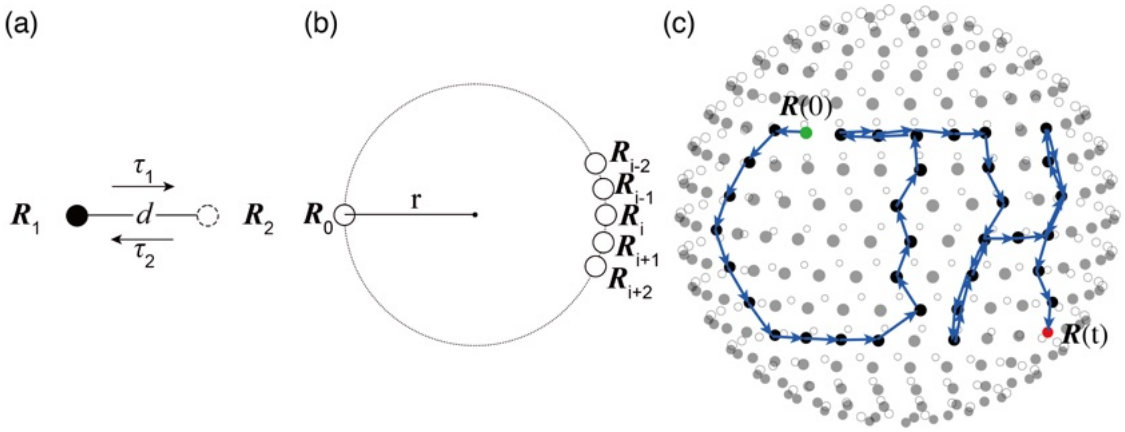


Figure 3.5: Diffusion models of (a) 2-site jump-diffusion, (b) N-fold jump diffusion on a circle, and (c) diffusion on a sphere. The hollow and solid circles represent a large enough amount of evenly distributed positions on the sphere, where the hollow circles represent the positions of the back of the sphere from this perspective, the blue arrows represent one of the random diffusion routes from the position at beginning $R(0)$ (green circle) to the position $R(t)$ (red circle) at time $t$.

## 3.2 X-ray diffraction

XRD is a technique for determining the crystal structure of materials. It utilizes coherent light from a source, typically gained by using the electron beam to hit a target material like copper (wavelength $\lambda \approx 1.54$ Å). When X-rays are incident on a material with an ordered periodic structure (*e.g.* crystal), diffracted light can result in a specific diffraction pattern, and then the structure of materials can be analyzed by collecting the pattern by the detector.

Unlike neutrons, X-rays interact with the electrons in the material rather than with the atomic nuclei. This difference in interaction means that the scattering cross-sections for different elements are different for X-rays and neutrons.

To better understand the working principle of XRD, we first need to understand the object of XRD analysis — the crystal. In the crystal, the parameters for a unit cell include the side length a, b, c, and angle $\alpha$, $\beta$, and $\gamma$ (Figure 3.6), where the electron density of a single crystal $\rho(\mathbf{r})$ can be found that has the periodic relation in three dimensions[88]:

$$\rho(\mathbf{r}) = \rho(\mathbf{r} + \mathrm{m}\mathbf{a} + \mathrm{n}\mathbf{b} + \mathrm{o}\mathbf{c}) \tag{3.17}$$

where m, n, and o are integers. Let $\mathrm{B} = [\mathbf{a}, \mathbf{b}, \mathbf{c}]$ as a basis, the Fourier transform $\mathrm{F}(\rho)$ can represent a function of reciprocal space with[88]:

$$F(\mathbf{B}) = \int_V \rho(\mathbf{r}) e^{2\pi i \mathbf{r}} dV \tag{3.18}$$

where V is the physical space. The diffracted intensity $\mathrm{I}(\mathbf{B}) \sim |F(\mathbf{B})|^2$ can be collected by the detector at a specific spatial angle. The vectors $\mathbf{a}^*, \mathbf{b}^*, \mathbf{c}^*$ can be defined as[88]:

$$\mathbf{a}^* = \frac{\mathbf{b} \times \mathbf{c}}{\mathbf{abc}}; \mathbf{b}^* = \frac{\mathbf{c} \times \mathbf{a}}{\mathbf{abc}}; \mathbf{c}^* = \frac{\mathbf{a} \times \mathbf{b}}{\mathbf{abc}} \tag{3.19}$$

are called the reciprocal lattice constants. From the Laue diffraction condition[88]:

$$I(\mathbf{B}) \neq 0 \text{ only if } \lambda\mathbf{Q} = \Delta\mathbf{B} = \mathrm{h}\mathbf{a}^* + \mathrm{k}\mathbf{b}^* + \mathrm{l}\mathbf{c}^* \tag{3.20}$$

the $Q$ is the momentum change from the original point O in the reciprocal space, and h, k, and l are integers. This can be visualized and explained by the Ewald diffraction condition [Figure 3.7(a)]. The $\mathbf{k}_\mathrm{i}$ represents the incident wavevector, and $\mathbf{k}_\mathrm{f}$ represents the diffracted wavevector, where $|\mathbf{k}| = 1/\lambda$ and $\lambda$ is the wavelength. Following the Laue condition[88]:

$$\mathbf{k}_\mathrm{f} = \mathbf{k}_\mathrm{i} + \mathbf{Q} \tag{3.21}$$

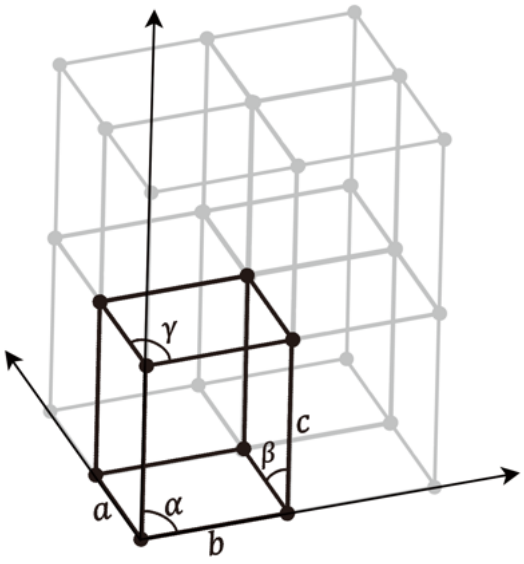


Figure 3.6: Schematic diagram of the unit cell.

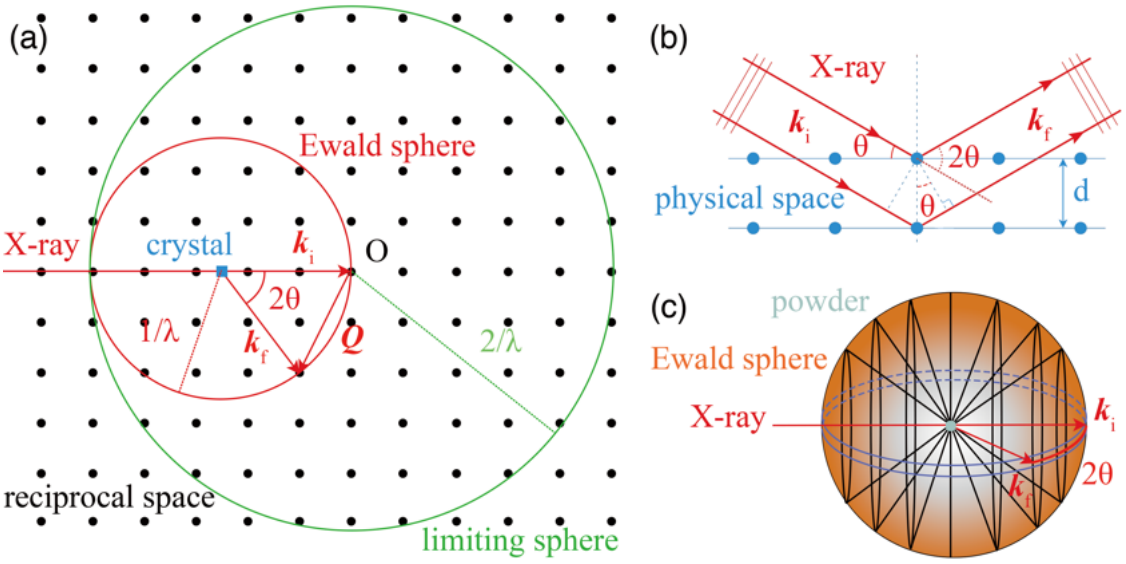


Figure 3.7: Schematic diagram of the Ewald sphere for (a) single crystal sample and (b) powder sample, and (c) is the schematic diagram of the Bragg's law.

thus the relationship between the diffraction angle $\theta$ and $Q$ can be easily found:

$$|\mathbf{Q}| = Q = 2\sin\theta/\lambda \tag{3.22}$$

therefore, in the physical space, the distance $d = 1/Q$ between the lattice plane can be found:

$$\lambda = 2d\sin\theta \tag{3.23}$$

this is the famous Bragg's law where $\theta$ is called the Bragg angle [Figure 3.7(b)]. The important property that follows the Laue-Bragg condition is the diffraction spectrum is related to a lattice plane in physical space. As known that $\sin\theta \leq 1$, $Q \leq 2/\lambda$ which is the limiting sphere range [Figure 3.7(a)].

### 3.2.1 Powder sample and single crystal sample

The principle of powder XRD (P-XRD) is the same as SC-XRD, both diffraction patterns follow the Laue-Bragg condition. The key difference between P-XRD and SC-XRD lies in the degree of texture of the sample. A pure single crystal has the highest degree of texture, which means the crystallographic orientation is anisotropic. In contrast, using the P-XRD usually assumes that the sample consists of many small crystallites randomly oriented in all directions, which means it is isotropic. Because of the random arrangement, a statistically significant number of crystal planes will be in the correct orientation to diffract X-rays at any given angle. Therefore, all planes in the crystal structure will contribute to the diffraction pattern, and the resulting data will show continuous diffraction rings instead of discrete spots, and the diffraction pattern is obtained by scanning different $2\theta$ angles [Figure 3.7(c)]. The P-XRD is suitable for samples that are not available as large single crystals. Furthermore, P-XRD measurement can also help identify the composition and content of impurities in samples by measuring enough amount of samples and refining the results.

Chapter 4

# Experimental details

This chapter gives a brief introduction to the facilities and instruments used, and to the procedures, analysis and processing of the results of the QENS and XRD experiments that have been performed in this thesis.

## 4.1 Quasielastic neutron scattering

### 4.1.1 FOCUS spectrometer

QENS experiments can be performed using several different types of instruments, including a spin-echo spectrometer, a backscattering spectrometer, and a time-of-flight (ToF) spectrometer. Utilizing different types of instruments enables the investigation of dynamics over a time range between $10^{-7}$ s to $10^{-13}$ s and a length scale from 0.1 to 1000 Å.[89] In this thesis, the ToF spectrometer FOCUS, which is located at the Swiss spallation neutron source (SINQ)* at the Paul Scherrer Institute in Switzerland, was used (Figure 4.1).

FOCUS is a time and space focusing ToF spectrometer, which uses both a Fermi-chopper and a monochromator for neutron beam focusing, for cold incident neutrons (Figure 4.2).[91,92] The broad band ("white") neutron beam is reduced in size by means of a vertically converging neutron guide, then chopped by a pre-selector disc chopper, reflected by a focusing monochromator crystal, and further chopped by a Fermi chopper to focus on the sample, making the incident neutron wavelength monochromized with confirmed incident neutron energy to the sample (Figure 4.2). By fixing the distance from the sample to the detector and recording the time-of-flight of the scattered neutrons as they reach the detector, the ToF spectrometer can calculate the speed of the scattered neutrons, thereby determining their energy after scattering. Additionally, using spatially distributed detectors, it can measure the neutron scattering angles, allowing for the calculation of the $E$ and $Q$ transfer.

Due to limitations such as neutron flux, the shape, size, and quantity of the samples are very important. Generally, the geometry of the sample is selected aiming at the scattering probability is less than 10%, thereby reducing the impact of multiple scattering and allowing the experiment to be conducted

*SINQ is the first and only continuous spallation neutron source in the world.[90]

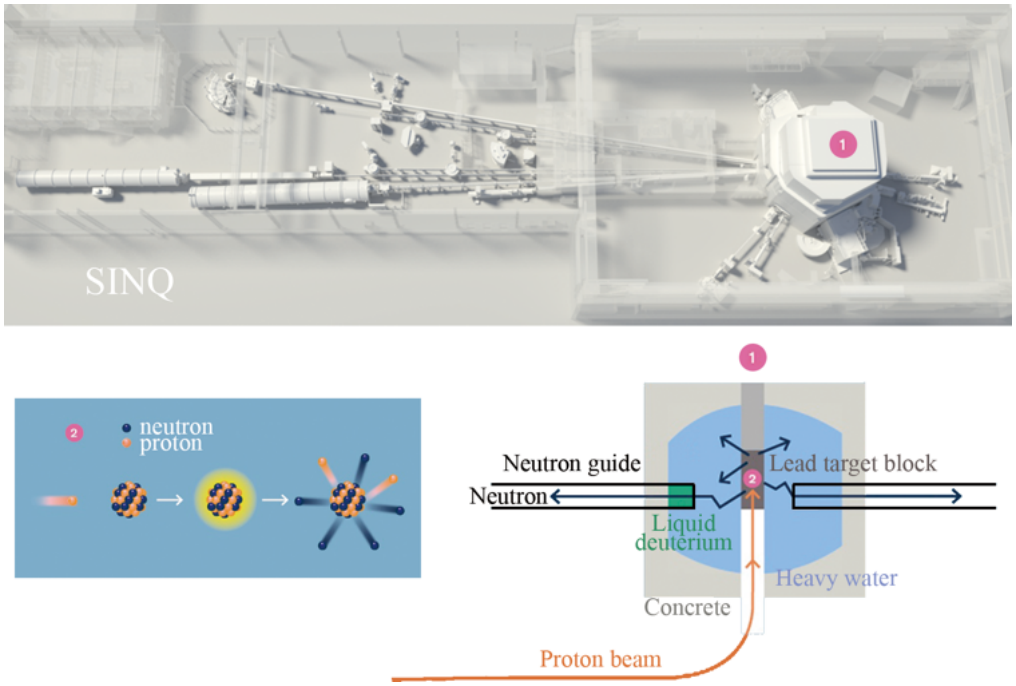


Figure 4.1: Schematic illustration of SINQ where (1) shows the neutron source, where the neutrons are transferred to each instrument by neutron guides, and (2) shows the mechanism of producing the neutron through proton beam and lead target. © 2024 PSI (Credit: Paul Scherrer Institute / Mahir Dzambegovic)

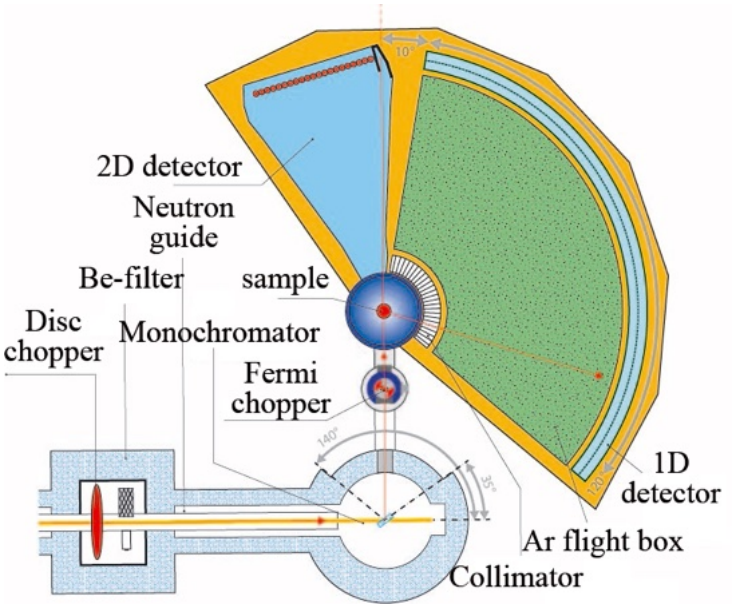


Figure 4.2: Schematic illustration of a ToF spectrometer - FOCUS.[93] © 2024 PSI (Credit: Paul Scherrer Institute)

within a controllable measuring time. A cylindrical aluminium sample cell, which has been chosen for my QENS experiments, is used to allow each neutron can pass a similar thickness of the sample during the scattering, whereas a flat cell might cause the neutron to go through more samples with a higher

probability of having multiple scattering when it is scattered to the angle parallel to the cell (Figure 4.3).

### 4.1.2 QENS data processing

The main goal of the QENS data processing is to obtain the dynamical structure factor $S(Q, E)$. This is obtained by a series of data reductions, calibrations, and corrections applied to the raw ToF data $N(2\theta,\ \mathrm{t})$. The main steps are described in the following and shown in Figure 4.4. Firstly, the measurement of an empty cell is subtracted from the raw data. Secondly, the data is normalized to the monitor counts. Thirdly, the efficiency of the detectors is corrected by measurement and subsequent normalization to a vanadium standard, which is an almost pure incoherent and elastic scatterer. Fourthly, the ToF raw data $N(2\theta,\ \mathrm{t})$ is transferred to the energy $(E)$ domain. Finally, the data is convoluted from the scattering angle to $Q$, thereby obtaining the structure factor $S(Q,E)$. Because the nature of scattering data is asymmetric, which can be briefly understood from the fact that a system at its ground state cannot find the energy to transfer to the neutrons, sometimes the process of detailed balance is necessary for this step to make the $S(Q,E)$ symmetrized to be fittable by the symmetric Lorentzians (see Appendix B.5).

Once the structure factor has been obtained, the evidence of the existence or non-existence of QENS can be found by comparison to the resolution function $R(Q,E)$. $R(Q,E)$ can be usually obtained by a measurement at a very low temperature (*e.g.* $T = 10$ K), where the scattering can be normally approximated as elastic. If a QENS signal is found, it can be usually analyzed by fitting to a sum of Lorentzians (see also section 3.1.4.1). The fitted $S(Q,E)$ needs to be convoluted with the $R(Q,E)$:

$$S(Q, E) \rightarrow [A_{i=0}(Q)\delta(E) + \sum_{i\neq 0} A_i(Q)\mathcal{L}_i(Q, E)] \circledast R(Q, E) \tag{4.1}$$

Sometimes, it is important to set a $E$ independent constant $bkg$ to represent the contribution from the tail of inelastic peak and the part from the dynamics

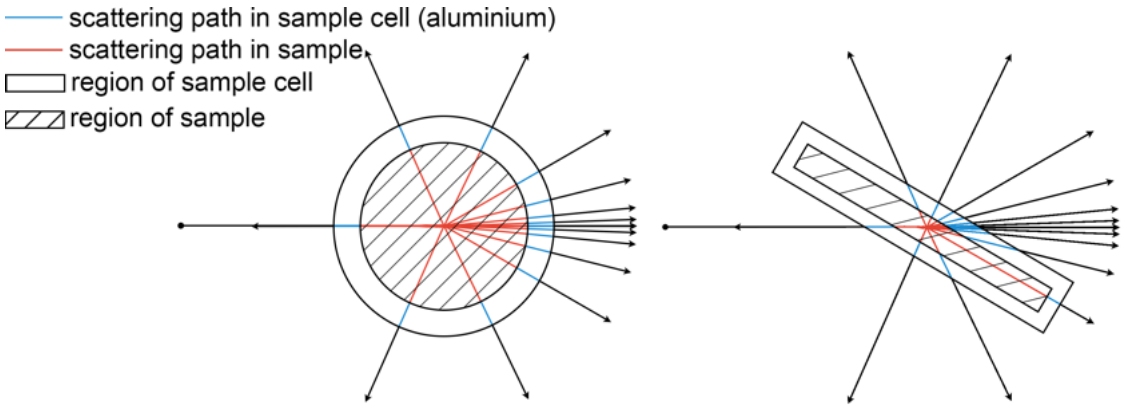


Figure 4.3: Schematic diagram of the sections of the cylindrical sample cell (left), flat sample cell (right), and the potential neutron scattering paths.

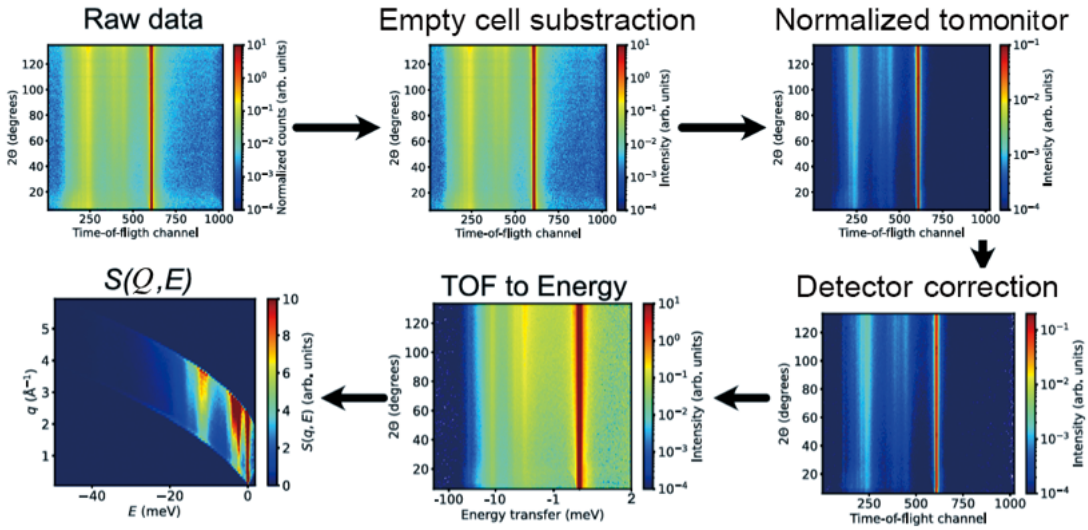


Figure 4.4: Flow chart of how the ToF data is corrected and reduced to $S(Q,E)$.[94] Used with permission of © Rasmus Lavén, 2023, from *Dynamical properties of metal halide and oxyhydride perovskite.* Doktorsavhandlingar vid Chalmers tekniska högskola, Ny series nr 5319.

that have shorter $\tau$ than the instrument time window. Then a fitted result can be collected for the QENS spectrum (example shown in Figure 4.5):

$$S(Q,E)_{\text{fitted}} = [A_0(Q)\delta(E) + \sum_{i\neq 0} A_i(Q)\mathcal{L}_i(Q,E) + bkg] \circledast R(Q,E) \qquad (4.2)$$

Fixed window scan (FWS) is a useful tool for analysis of the temperature dependence of QENS intensity. It can be obtained through a series of temperature scans over a specific energy transfer range which can give an

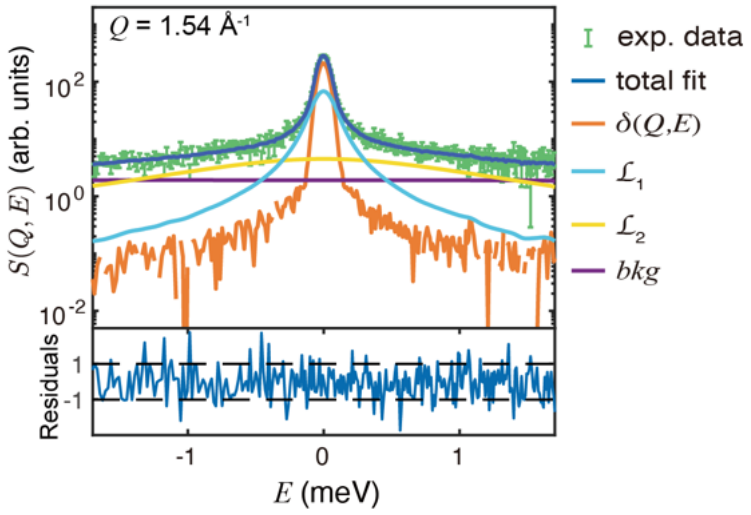


Figure 4.5: $S(Q,E)$ fitting example from the Paper 3 on $FASnCl_3$ at $Q$ = 1.54 Å$^{-1}$, residual = $[S(Q,E)_{\text{fitted}} - S(Q,E)_{\text{exp.}}]/S(Q,E)_{\text{exp.error}}$.

overview of the dynamics of a sample. Experimentally, FWS can be measured by backscattering spectrometers through the monochromator to choose the neutron wavelength, or it can be obtained by $\theta$-integrated ToF spectrometer data. Elastic fixed window scans (EFWSs) can show the onset of motion whose correlation time is within the instrumental time window (Figure 4.6). The linear decreasing of EFWSs is from the mean square displacement $\langle u^2 \rangle(T)$ of atomic thermal vibration described by Debye-Waller factor[87]:

$$DWF = e^{-Q^2 \langle u^2 \rangle} \tag{4.3}$$

## 4.2 XRD

### 4.2.1 XtaLAB Synergy-R Xray diffractometer

For the XRD measurements performed in the scope of this thesis, the single crystal X-ray diffractometer XtaLAB Synergy-R from Rigaku which is located in the Chalmers Materials Analysis Laboratory (CMAL) was used (Figure 4.7). For this instrument, the ideal crystal size is around several dozen micrometres. Under a microscope, silicone oil was used to attach the crystal to the crystal holder for the experiments. The crystal holder and a 2D detector work together through rotation to gain the entire reciprocal lattice information within the limiting sphere. After obtaining a clear crystal diffraction pattern (dots/peaks without ring), the diffraction data was imported into the crystallographic software package Olex2 to solve and visualize the structure (Figure 4.8).[92] It is important to note that although SCXRD is a powerful tool for crystal structure analysis, due to the complexity of crystal structures, a crystal's structure which is based solely on SC-XRD results cannot be fully determined. A relatively

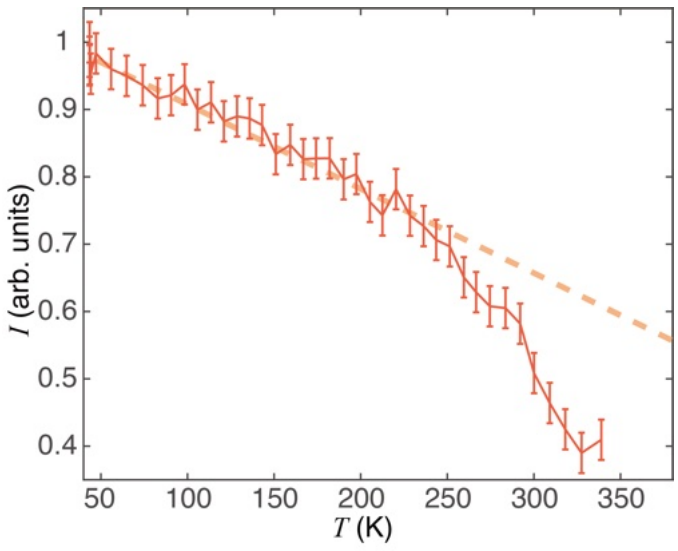


Figure 4.6: EFWSs example from Paper 3 $MBAMnCl_3$ sample where the dashed straight line can be described by Debye-Waller factor.

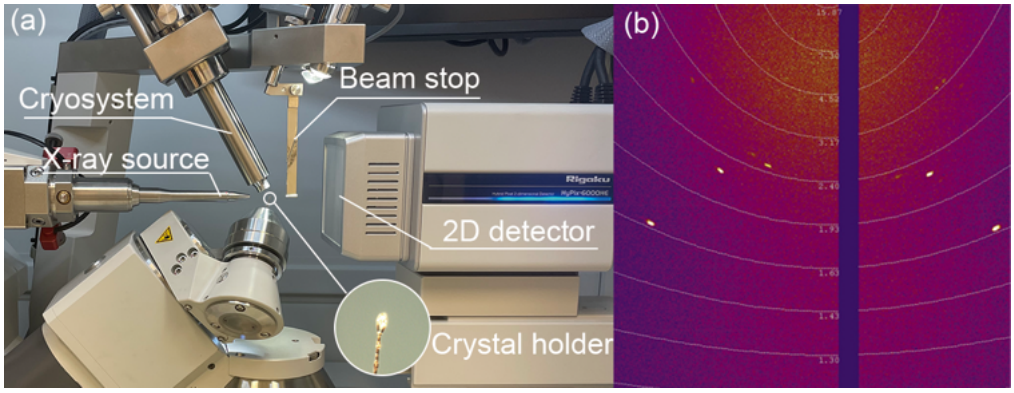


Figure 4.7: (a) The photo of high-flux rotating anode X-ray diffractometer XtaLAB Synergy-R at CMAL, and (b) one of the diffraction patterns of $MBAMnCl_3 \cdot C_2H_5OH$ sample.

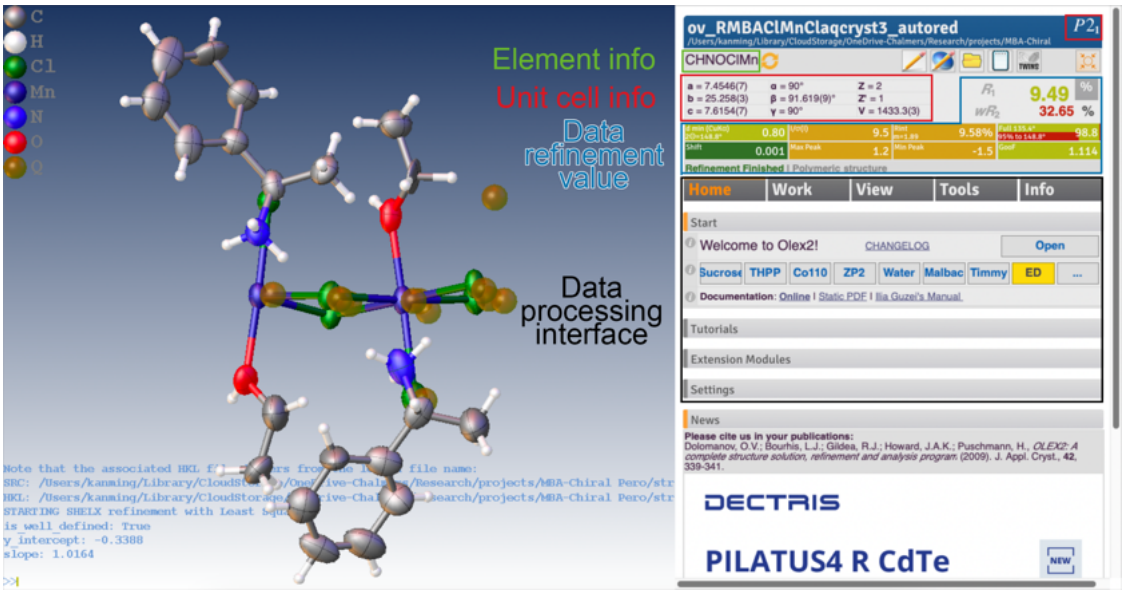


Figure 4.8: The graphical user interface of the crystallographic software package Olex2.

reliable result requires comprehensive analysis, incorporating knowledge of the sample's elemental composition and other information based on chemical theory. Additionally, comparing data with crystal databases can also help analyze and confirm the structural information of the sample.

### 4.2.2 Bruker D8 Discover X-ray diffractometer

For the P-XRD experiments, the X-ray diffractometer Bruker D8 Discover was used (Figure 4.9) which is also from the CMAL. Unlike SC-XRD, because using the powder sample, the sample platform in the PXRD instrument maintains a fixed horizontal position. The diffraction pattern is obtained by simultaneously changing the X-ray incident angle and the detector angle along the $2\theta$. The sample is scanned by setting the starting and final $2\theta$ angles and the rotation

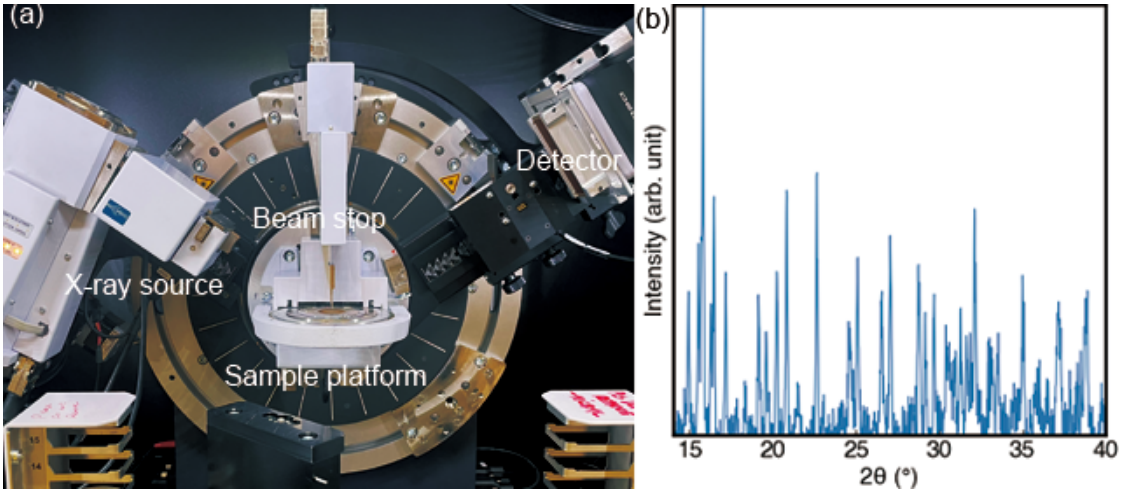


Figure 4.9: (a) X-ray diffractometer Bruker D8 Discover with powder sample platform kit from the CMAL, and (b) the XRD pattern of R-MBAMn$Cl_3$·2$H_2O$ sample.

speed. The scanning time is usually shorter than SC-XRD due to the larger sample quantity. Since there are fewer characteristic peaks, P-XRD is mainly used for comparative confirmation of the sample's crystal structure. In the presence of extra peaks, it can also help to identify impurities in the sample.

Chapter 5

# Results and discussion

This chapter begins with a brief summary of the appended papers and finishes with a collective discussion of the results with a focus on how these results add to the current literature on dynamics in MHPs.

## 5.1 Rotational dynamics of FA cations in $FASnCl_3$, $FASnBr_3$, and $FA_2SnI_6$ (Paper I)

To better understand the nature of the dynamics of FA cations in tin-based (lead-free) MHPs, $FASnCl_3$, $FASnBr_3$, and $FA_2SnI_6$ have been measured by using QENS at FOCUS, PSI. A series of temperature-dependent QENS signals has been probed from these samples (Figure 5.1). The EFWSs (elastic fixed window scans) reveal the onset temperature of FA cation localized dynamics in $FASnBr_3$ and $FA_2SnI_6$ is at around 150 K, and for $FASnCl_3$ is at around 250 K. Besides the different dynamics onset temperature, it can be observed that the QENS intensity for $FA_2SnI_6$ increases sharply between 200 and 225 K, for $FASnBr_3$ between 200 and 250 K, whereas for $FASnCl_3$ remains low below 300 K but becomes observable from 350 K (Figure 5.1).

From the $Q^2$ independent behaviour of the FWHM of the fitted QENS

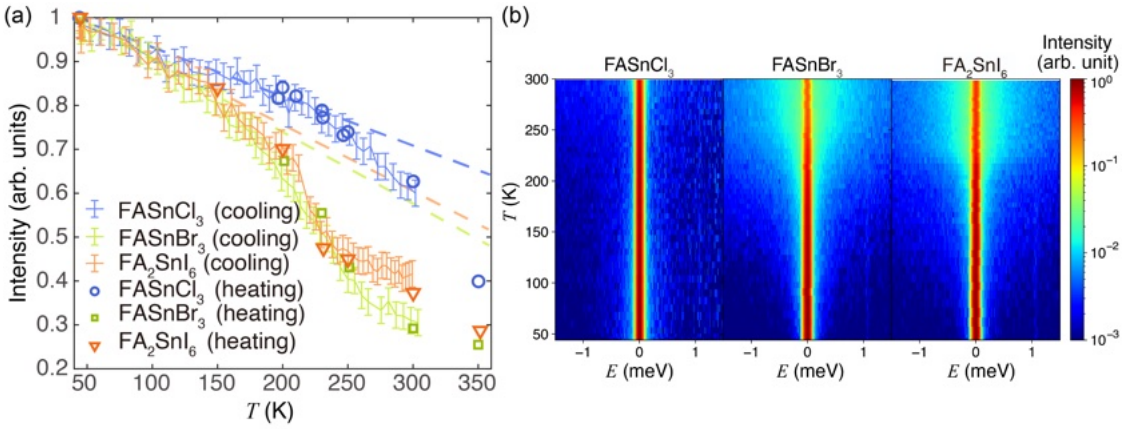


Figure 5.1: (a) EFWSs, and (b) temperature-dependent $E$ distributed neutron scattering intensity $I(T,E)$ heatmaps of $FASnCl_3$, $FASnBr_3$ and $FA_2SnI_6$.

signal one can understand that the dynamics are localized in nature. The FWHM of the narrower Lorentzian ($\mathcal{L}_1$) from the fitting is around 0.1 – 0.5 meV, which translates into a timescale of the FA localized diffusion a few picoseconds. An Arrhenius fit of the temperature-dependent FWHM suggests an activation energy of 66±8 meV for $FASnBr_3$ and 50±8 meV for $FA_2SnI_6$.

Through the QENS fitting, 2- and 4-fold jump diffusion and isotropic reorientation models (Figure 5.2a) have been built up for $FASnBr_3$ and $FA_2SnI_6$ of their tetragonal phase (∼150 – 200 K) and cubic phase (∼230 – 350 K). The 24-site jump-diffusion model fits the data worse than the isotropic reorientation model (Figure 5.2b) This important result indicates that the influence of hydrogen bonds (which have directionality and can force hydrogens to point to halide ions) to FA cation rotational diffusion becomes weaker than in the orthorhombic phase in the cubic phase of $FASnBr_3$ and $FA_2SnI_6$ , which could because of higher unit cell volume (longer and weaker hydrogen bond) bringing lower energy barrier for FA cation diffusion and FA cation having higher thermal energy in cubic phase.

From the QENS results, one can conclude that the dynamical property of FA cation in the tin-based MHP system is dependent on the halide ion. With a longer halide ion radius [$r_{I^-}$ (206 pm) > $r_{Br^-}$ (182 pm) > $r_{Cl^-}$ (167 pm)] [95]

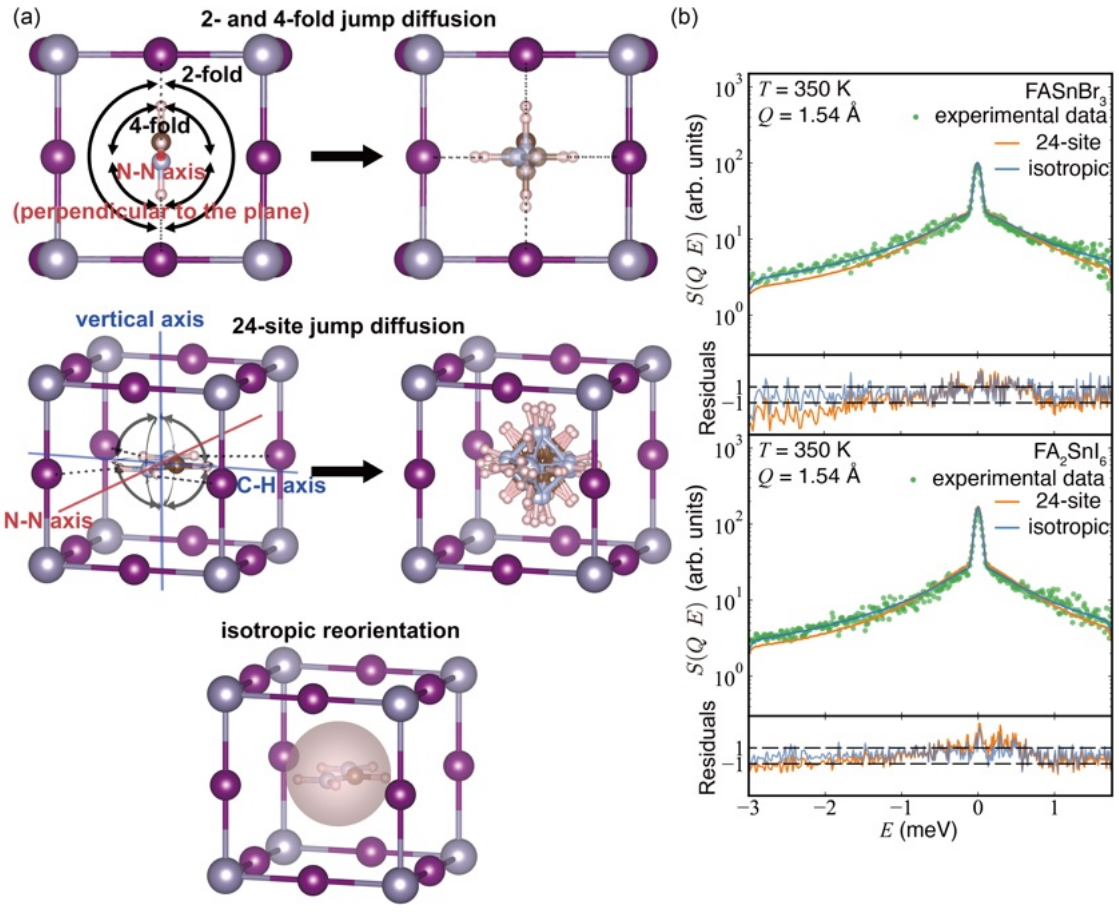


Figure 5.2: (a) Schematic illustration of rotational motion models of the FA cation, and (b) $S(Q, E)$ fitting of $FASnBr_3$, and $FA_2SnI_6$ at 350 K, $Q = 1.54$ Å.

and a larger unit cell [$a$[$Sn_{0.5}I_3$] (6.17 Å)[79] $\gtrsim$ $a$[$SnBr_3$] (6.03 Å)[96] $\gtrsim$ $a$[$SnCl_3$] (5.79 Å, non-cubic)[97]], the tin-based perovskite can have a stronger QENS intensity at the same temperature. Reflected on the cation dynamics, this represents FA cations can have a faster and higher spatial freedom level of the localized diffusion with a larger halide ion and the same B-site cation in MHPs.

Compared to FAPb$X_3$ ($X$= Br, and I), the localized diffusional dynamics of FA cations are of tin-based perovskite at cubic phase have a similar timescale at 300 K (FAPb$I_3$: 1.26 ps,[28] FAPb$Br_3$: 5.6 ps[50]), and similar activation energy level in the cubic phase (FAPb$I_3$: 52 ± 6 meV,[98] FAPb$Br_3$: 61.8 ± 5 meV[50]), and the same isotropic reorientation geometry to the lead-based perovskite (comprehensive comparison can be found in the SI of Paper 1 Table S2). These results reveal that there is no direct interaction between the organic cations dynamics and the B-site divalent metal cation, but that the organic cation dynamics highly depend on the type of halide anion.

## 5.2 Structure and organic cation dynamics in MBAMnCl$_3$ (Paper II&III)

As a technique based on the fitting of elastic peak broadening, QENS analysis relies on finding reasonable motion models which highly depend on the sample's structural properties. In order to get a better understanding of the MBA rotational dynamics properties in the novel MHP MBAMn$Cl_3$, it is necessary to determine the crystal structure while the reported structure has an unneglectable, and crystallographically unacceptable large uncertainty in the lattice parameter $a$ = 6 (2) Å.

A better SC-XRD result with higher accuracy of MBAMn$Cl_3$·2$H_2$O monoclinic ($P2_1$) phase is obtained by our measurement (Figure 5.3a). Furthermore, the SC-XRD result from the same batch of samples but different crystals show a new monoclinic ($P2_1$) phase with ethanol ligands where the chemical formula is MBAMn$Cl_3$·$C_2H_5$OH (Figure 5.3b). Interestingly, a similar but chloride-based perovskite system also has both 1D and 0D structures where the transformation is because of the change in environment humidity.[99] This new phase might be transferred from MBAMn$Cl_3$·2$H_2$O because of the different environments of storage and XRD sample preparation. However, P-XRD results show the main component of the crystals in the sample should still be MBAMn$Cl_3$·2$H_2$O dimer structure. Therefore, the QENS analysis on this sample is still based on the MBAMn$Cl_3$·2$H_2$O phase but with better quality of the structure information.

Building on our XRD structural study of MBAMn$Cl_3$·2$H_2$O, we investigated the dynamics of the MBA cation by QENS at FOCUS, PSI. Figure 5.4(a) is the EFWSs result which shows similar temperature intensity changes for two samples upon heating and the onset of MBA diffusional dynamics can be found at around 275 K. Interestingly, comparing the EFWSs (elastic fixed windows scans) data upon heating with the data upon cooling, the thermal hysteresis of the elastic scattering intensity can be found from both samples (Figure 5.4a), and the full map of scattering temperature scans during cooling (Figure 5.4b) shows the R-MBAMn$Cl_3$·2$H_2$O has a larger hysteresis than S-MBAMn$Cl_3$·2$H_2$O.

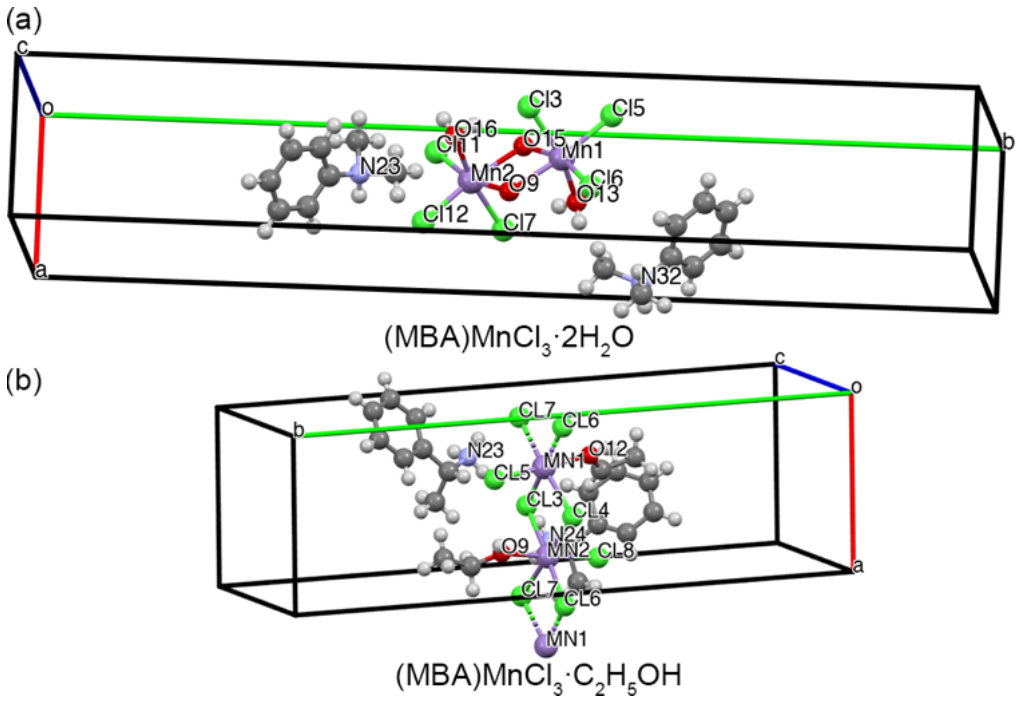


Figure 5.3: A view of the molecular crystal structure of (a) $MBAMnCl_3{\cdot}C_2H_5OH$ 1 at 107 K, and (b) $MBAMnCl_3{\cdot}2H_2O$ at 100 K. The dark grey spheres represent the carbon atoms and the light grey spheres represent the hydrogen atoms.

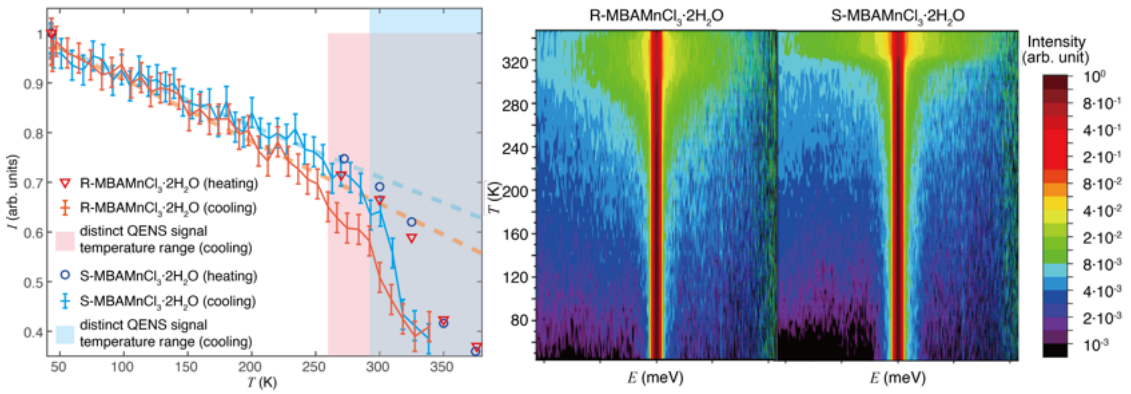


Figure 5.4: (a) EFWSs, and (b) temperature-dependent $E$ distributed neutron scattering intensity $I(T,E)$ heatmaps of $FASnCl_3$, $FASnBr_3$ and $FA_2SnI_6$.

The key result of the geometry of the MBA cation dynamics is obtained from the EISF (elastic incoherent structure factor) fitting. A series of dynamical models which can fit the experimental data have been used, *i.e.* the jump-diffusion and rotational diffusion for the function groups (*e.g.* $-NH_3$, $-CH_3$, and $-C_6H_5$), and the model at a higher temperature ($\geq 350$ K) where the whole cation can have another rotation axis and hydrogens have biaxial rotational dynamics (Figure 5.5). The onset of methyl and ammonium 3-fold jump diffusion of MBA cation from $MBAMnCl_3{\cdot}2H_2O$ occurs at 270 K, and the 2-fold jump diffusion of phenyl could occur at 325 K. The QENS intensity increases rapidly from 325

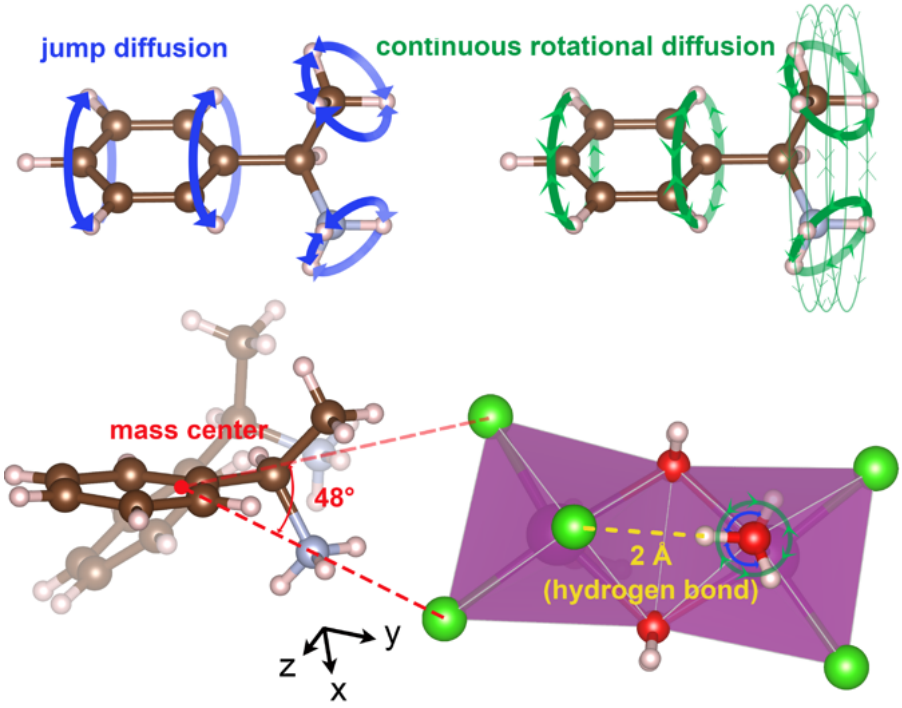


Figure 5.5: Schematic illustration of function groups (*e.g.* -$NH_3$, -$CH_3$, and -$C_6H_5$) jump-diffusion model, continuous rotational diffusion model, and whole cation $C_2$ jump-diffusion model.

to 350 K. At temperatures above 350 K, the dynamics become more complex, it has been considered as biaxial rotational diffusion where the second axis passes through the MBA mass centre and is perpendicular to the plane containing the mass center and the two closest halide ions (Figure 5.5). The rotation angle of 48° comes from the angle of <Cl - mass center - Cl> (Figure 5.5).

Compared to the other low-dimensional MHPs which also have relatively larger organic cations (ionic radius larger than $\sqrt{3}$ × B-X bond length),[57,71] MBA also show localized function group's rotational dynamics in $MBAMnCl_3{\cdot}2H_2O$, but at higher temperature, MBA can have whole cation $C_2$ rotational diffusion which has not been reported from QENS study. The more complicated dynamics with a higher spatial freedom level could be led by the smaller energy barrier of MBA cation localized rotational diffusion, since each organic cation in semi-0D $MBAMnCl_3{\cdot}2H_2O$ is surrounded by less amount of halide ion than in other 2D MHPs in the same voltage of crystal.

## 5.3 Discussion

Comparing all these different MHPs, it is obvious that all the localized rotational dynamics from the different organic cations are highly temperature-dependent. Generally, the timescale of the dynamic becomes shorter and the geometry becomes more complex with higher spatial freedom at a higher temperature. The exception can be found from the $FASnBr_3$, where the geometry transforms from jump diffusion to isotropic reorientation from 200 K to 230 K and the

timescale is increased from 1 to 3 ps. This may be because the different geometry can bring new rotation axes which makes competition with the dynamics at lower temperatures.

As we can find from the QENS results from FA tin-based MHPs, the halide ion can affect the organic cation's rotational diffusion. The interaction between the organic cation and inorganic framework has been reported to rely on the dipole-dipole interaction (has been reported as hydrogen bonding) between the function group (*e.g.* -$NH_3$) from the organic cation and the halide ion.[100–103] Comparing the FA-based MHPs to the MA-based MHPs,[24,25] FA which shows isotropic reorientation has higher spatial freedom than MA with $C_3 \otimes C_4$ rotational diffusion. This may be because the FA has less polarity than MA which has weaker dipole dipole interaction with the inorganic framework (less energy barrier). Comparing the MBA$MnCl_3 \cdot 2H_2O$ to the other low-dimensional MHP with a larger cation (*e.g.* OA,[71] ODA, nBA, and GABA[57]) than MA and FA, MBA$MnCl_3 \cdot 2H_2O$ can have multiaxial whole-cation rotational diffusion but the other cations can only have function group's localized diffusion. This might rely on the fact that MBA is surrounded by fewer halide ions because of the 0D MHP structure where the energy barrier for organic cation dynamics is smaller.

Chapter 6

# Outlook and future work

In my future work, I plan to focus on the direct impact of cation-localized rotational dynamics on the photoelectric conversion efficiency of MHPs. Therefore, I will further discuss how the cation's localized dynamics influence the formation of polarons* when the excitons are generated in MHPs by incident light (Figure 6.1). Specifically, many studies support that in MHPs, photo-generated charge carriers can couple with the polarization fields of the distorted lattice, resulting in the formation of polarons.[36,39,105,106] The polaron can protect the energetic carriers that come from the molecular dipoles that screen their scattering with longitudinal optical phonons to extend the exciton lifetime and diffusion length. Many studies reported the dynamics of the monovalent cation play a crucial role in polaron formation and hopping. The exciton-caused changes of cation dynamical properties can influence the local lattice distortions and, in turn, help MHP form the polaron and then affect carrier

*A polaron is a quasiparticle used to describe the interactions between electrons and atoms in a solid material that manifests as a localized spatial redistribution of atoms and electric fields.

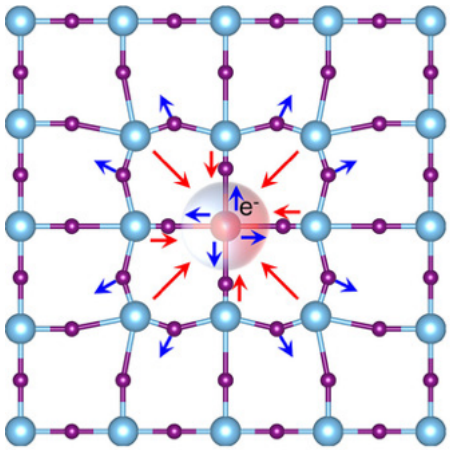


Figure 6.1: Schematic illustration of a polaron, where the blue spheres represent the cations, purple spheres represent the anions, and the red and blue arrows represent attractive and repulsive electrical forces from the electron to the ions, respectively.[104]

mobility.[18,69,107–109] Based on density functional theory and other calculations,[39,110] experimental work on the rotor-lattice deformation-polaron-carrier mobility theory mostly involves infrared/time-resolved infrared measurements to obtain information on the vibrations of MA (C-H, N-H stretching) and lattice distortions in $MAPbI_3$.[49,106,111]

In order to get more insights into this theory, I will design a series of QENS and inelastic neutron scattering (INS) experiments on MHPs in the photoexcited state to explore the relationship between cation localized rotational dynamics and factors such as polaron formation and lifetime. Compared to IR or NMR, the QENS technique can directly probe the difference in cation's reorientation mean residence time between in dark environment state (picoseconds) and optically excited state (MA would like to reorientate to point to the carrier and the carrier lifetime is in nanoseconds) to support the theory and simulation results. Besides the QENS, the INS technique can measure the lower energy ($E<$ 20 meV) vibration modes from MA. These low-energy librational phonons are highly related to the lattice distortion[112] which also can be powerful evidence for the relation of inorganic lattice and organic cation to polaron. Through these experiments, the formation of polaron and the relationship between organic cation localized dynamics and polaron will be further demonstrated.

Chapter 7

# Summary and Conclusions

In conclusion, my study of $FASnX_3$ ($X$ = Cl, Br) and $FA_2SnI_6$ has unravelled the localized diffusional dynamical properties of FA cations, such as the onset of localized rotational dynamics of FA cations, at around 150 K for $FASnBr_3$ and $FA_2SnI_6$, and 250 K for $FASnCl_3$. For $FASnBr_3$ and $FA_2SnX_6$ at relatively low temperatures ($T \leq$200 K) the dynamics can be generally described as 2-fold and 4-fold jump diffusional dynamics of the FA cations, whereas at higher temperatures (230 K$\leq T \leq$350 K), the dynamics of the FA cations can be considered as isotropic reorientation of the FA cation. The activation energy of the FA isotropic reorientation is around 40–80 meV with different halide ions.

For the chiral perovskite $MBAMnCl_3$, My studies unravel the localized diffusional dynamical properties of MBA cations, such as the onset temperature of rotational diffusion of -$NH_3$ and -$CH_3$ is 270 K, and for the -$C_6H_5$ is 300 K. The onset temperature of multiaxial rotational diffusion of hydrogens is around 350 K. This represents that, at low temperatures, the hydrogens from the MBA cation have rotational diffusion by the functional groups (-$NH_3$, -$CH_3$, and -$C_6H_5$), and at higher temperatures, the whole MBA cation can have the $C_2$ jump diffusion where the hydrogens can have the second rotation axis. Furthermore, the structure properties of $MBAMnCl_3{\cdot}C_2H_5OH$ and $MBAMnCl_3{\cdot}2H_2O$ have been investigated through SC-XRD. The P-XRD results show the dominant structure is the dimer $MBAMnCl_3{\cdot}2H_2O$.

These studies of different organic cations' localized diffusional dynamics in different dimensional MHPs clearly show that all these dynamics are highly temperature-dependent where the localized diffusional dynamics are thermal energy driven. These localized diffusional dynamics also highly depend on the organic cations themselves, and halide anions. It indicates that with smaller organic cations' moments of inertia, smaller chemical polarity, and smaller diffusion energy barriers (from the localized electric field distribution, commonly determined by the hydrogen bond strength), organic cation dynamics in MHPs tend to have higher spatial freedom and faster diffusion rates. These new QENS research on MHPs shows that the thermal-driven organic cation rotational diffusion in MHPs is affected by the complex coupling and competition mechanisms between the organic cations, the halide ions and the inorganic framework structures.

In the future, I plan to focus on investigations of a more direct relationship between the organic cation dynamics and the MHPs' great optoelectronic properties by setting a series of neutron scattering experiments to investigate the role of the organic cations in the MHPs' polaron formation and immigration.

# Acknowledgment

Firstly, I would like to thank my supervisor Maths Karlsson, for giving me the opportunity to join this interesting Ph.D. project and for his great support in scientific research and academic writing. I would also like to thank my vice supervisor Feng Gao for his support and advice in sample preparation and material science. I would like to thank my examiner Bo Albinsson and my study director Itai Panas for their mature and wise study guidance, advice, and knowledge sharing. I would also like to thank my manager Henrik Leion, and administrator Sandra Nayeri for their help in my study in Chalmers. I would like to thank my collaborators Lars Öhrström, Lorenzo Malavasi, Weidong Cai, Fanni Juranyi, Michael Koza, Markus Appel, Masato Matsuura, and Hiromu Tamatsukuri for all their help in science research, neutron experiment, and sample preparation. I would also like to thank my group mates and friends in Chalmers Rasmus Lavén, Elena Naumovska, Lucas Fine, Aymen Yangui, Peng Pan, Pedram Pakmehr, Joanna Jedon, Oskar Öjstedt for sharing the happiness, cookies and beer. I would like to thank my office mates Christine Geers, Maria Olausson, Amanda Persdotter, Anton Chyrkin and everyone in OOMK. I would also like to thank all my friends from the SwedNESS. Finally, I would like to give big thanks to all my family and friends around the world.

# Bibliography

[1] S. D. Stranks and H. J. Snaith, Metal-halide perovskites for photovoltaic and light-emitting devices. *Nat. Nanotechnol.*, 2015, **10**, 391–402.

[2] A. Fakharuddin, M. K. Gangishetty, M. Abdi-Jalebi, S.-H. Chin, A. R. bin Mohd Yusoff, D. N. Congreve, W. Tress, F. Deschler, M. Vasilopoulou and H. J. Bolink, Perovskite light-emitting diodes. *Nat. Electron.*, 2022, **5**, 203–216.

[3] J. H. Heo, S. H. Im, J. H. Noh, T. N. Mandal, C.-S. Lim, J. A. Chang, Y. H. Lee, H.-j. Kim, A. Sarkar, M. K. Nazeeruddin, M. Grätzel and S. I. Seok, Efficient inorganic–organic hybrid heterojunction solar cells containing perovskite compound and polymeric hole conductors. *Nat. Photonics*, 2013, **7**, 486–491.

[4] Y. Rong, Y. Hu, A. Mei, H. Tan, M. I. Saidaminov, S. I. Seok, M. D. McGehee, E. H. Sargent and H. Han, Challenges for commercializing perovskite solar cells. *Science*, 2018, **361**, 6408.

[5] *Best Research-Cell Efficiency Chart*, 2023, `www.nrel.gov/pv/cell-efficiency.html`.

[6] J.-W. Lee, S. Seo, P. Nandi, H. S. Jung, N.-G. Park and H. Shin, Dynamic structural property of organic-inorganic metal halide perovskite. *iScience*, 2021, **24**, 101959.

[7] V. Goldschmidt, Die Gesetze der Krystallochemie. *Naturwissenschaften*, 1926, **14**, 477–485.

[8] H. Megaw, Crystal Structure of Barium Titanate. *Nature*, 1945, **155**, 484–485.

[9] S. D. Stranks, Nonradiative Losses in Metal Halide Perovskites. *Acs Energy Lett.*, 2017, **2**, 1515–1525.

[10] S. Rühle, Tabulated values of the Shockley–Queisser limit for single junction solar cells. *Sol. Energy*, 2016, **130**, 139–147.

[11] J.-H. Wei, X.-D. Wang, J.-F. Liao and D.-B. Kuang, High Photoluminescence Quantum Yield (>95%) of $MAPbBr_3$ Nanocrystals via Reprecipitation from Methylamine-$MAPbBr_3$ Liquid. *ACS Appl. Electron. Mater.*, 2020, **2**, 2707–2715.

[12] S. D. Stranks, V. M. Burlakov, T. Leijtens, J. M. Ball, A. Goriely and H. J. Snaith, Recombination Kinetics in Organic-Inorganic Perovskites: Excitons, Free Charge, and Subgap States. *Phys. Rev. Appl.*, 2014, **2**, 034007.

[13] P. J. Cegielski, A. L. Giesecke, S. Neutzner, C. Porschatis, M. Gandini, D. Schall, C. A. R. Perini, J. Bolten, S. Suckow, S. Kataria, B. Chmielak,

T. Wahlbrink, A. Petrozza and M. C. Lemme, Monolithically Integrated Perovskite Semiconductor Lasers on Silicon Photonic Chips by Scalable Top-Down Fabrication. *Nano Lett.*, 2018, **18**, 6915–6923.

[14] Q. Zhang, Q. Shang, R. Su, T. T. H. Do and Q. Xiong, Halide Perovskite Semiconductor Lasers: Materials, Cavity Design, and Low Threshold. *Nano Lett.*, 2021, **21**, 1903–1914.

[15] Q. Shang, M. Li, L. Zhao, D. Chen, S. Zhang, S. Chen, P. Gao, C. Shen, J. Xing, G. Xing, B. Shen, X. Liu and Q. Zhang, Role of the Exciton–Polariton in a Continuous-Wave Optically Pumped $CsPbBr_3$ Perovskite Laser. *Nano Lett.*, 2020, **20**, 6636–6643.

[16] G. Maculan, A. D. Sheikh, A. L. Abdelhady, M. I. Saidaminov, M. A. Haque, B. Murali, E. Alarousu, O. F. Mohammed, T. Wu and O. M. Bakr, $CH_3NH_3PbCl_3$ Single Crystals: Inverse Temperature Crystallization and Visible-Blind UV-Photodetector. *J. Phys. Chem. Lett.*, 2015, **6**, 3781–3786.

[17] Q. Lin, A. Armin, P. L. Burn and P. Meredith, Near infrared photodetectors based on sub-gap absorption in organohalide perovskite single crystals. *Laser Photonics Rev.*, 2016, **10**, 1047–1053.

[18] H. Zhang and N.-G. Park, Polarons in perovskite solar cells: effects on photovoltaic performance and stability. *J. Phys.: Energy*, 2023, **5**, 024002.

[19] L. Mao, C. C. Stoumpos and M. G. Kanatzidis, Two-Dimensional Hybrid Halide Perovskites: Principles and Promises. *J. Am. Chem. Soc.*, 2019, **141**, 1171–1190.

[20] Z. Yuan, C. Zhou, Y. Tian, Y. Shu, J. Messier, J. C. Wang, L. J. van de Burgt, K. Kountouriotis, Y. Xin, E. Holt, K. Schanze, R. Clark, T. Siegrist and B. Ma, One-dimensional organic lead halide perovskites with efficient bluish white-light emission. *Nat. Commun.*, 2017, **8**, 14051.

[21] M. I. Saidaminov, J. Almutlaq, S. Sarmah, I. Dursun, A. A. Zhumekenov, R. Begum, J. Pan, N. Cho, O. F. Mohammed and O. M. Bakr, Pure $Cs_4PbBr_6$: Highly Luminescent Zero-Dimensional Perovskite Solids. *Acs Energy Lett.*, 2016, **1**, 840–845.

[22] M. T. Weller, O. J. Weber, P. F. Henry, A. M. Di Pumpo and T. C. Hansen, Complete structure and cation orientation in the perovskite photovoltaic methylammonium lead iodide between 100 and 352 K. *Chem. Commun.*, 2015, **51**, 4180–4183.

[23] D. H. Fabini, C. C. Stoumpos, G. Laurita, A. Kaltzoglou, A. G. Kontos, P. Falaras, M. G. Kanatzidis and R. Seshadri, Reentrant Structural and Optical Properties and Large Positive Thermal Expansion in Perovskite Formamidinium Lead Iodide. *Angew Chem Int Edit*, 2016, **55**, 15392–15396.

[24] T. Chen, B. J. Foley, B. Ipek, M. Tyagi, J. R. Copley, C. M. Brown, J. J. Choi and S. H. Lee, Rotational dynamics of organic cations in the $CH_3NH_3PbI_3$ perovskite. *Phys. Chem. Chem. Phys.*, 2015, **17**, 31278–86.

[25] A. M. Leguy, J. M. Frost, A. P. McMahon, V. G. Sakai, W. Kockelmann, C. Law, X. Li, F. Foglia, A. Walsh, B. C. O'Regan, J. Nelson, J. T. Cabral and P. R. Barnes, Corrigendum: The dynamics of methylammonium ions in hybrid organic-inorganic perovskite solar cells. *Nat. Commun.*, 2015, **6**, 7780.

[26] V. K. Sharma, R. Mukhopadhyay, A. Mohanty, V. G. Sakai, M. Tyagi and D. D. Sarma, Contrasting Effects of FA Substitution on MA/FA Rotational Dynamics in $FA_xMA_{1-x}PbI_3$. *J. Phys. Chem. C*, 2021, **125**, 13666–13676.

[27] V. K. Sharma, R. Mukhopadhyay, A. Mohanty, V. García Sakai, M. Tyagi and D. D. Sarma, Influence of the Halide Ion on the A-Site Dynamics in $FAPbX_3$ (X = Br and Cl). *J. Phys. Chem. C*, 2022, **126**, 7158–7168.

[28] R. Lavén, M. M. Koza, L. Malavasi, A. Perrichon, M. Appel and M. Karlsson, Rotational Dynamics of Organic Cations in Formamidinium Lead Iodide Perovskites. *J. Phys. Chem. Lett.*, 2023, **14**, 2784–2791.

[29] S. Ghimire and C. Klinke, Two-dimensional halide perovskites: synthesis, optoelectronic properties, stability, and applications. *Nanoscale*, 2021, **13**, 12394–12422.

[30] L. Zhang, Y. Liu, Z. Yang and S. Liu, Two dimensional metal halide perovskites: Promising candidates for light-emitting diodes. *J. Energy Chem.*, 2019, **37**, 97–110.

[31] G. Long, R. Sabatini, M. I. Saidaminov, G. Lakhwani, A. Rasmita, X. Liu, E. H. Sargent and W. Gao, Chiral-perovskite optoelectronics. *Nat. Rev. Mater.*, 2020, **5**, 423–439.

[32] J. Ma, H. Wang and D. Li, Recent Progress of Chiral Perovskites: Materials, Synthesis, and Properties. *Adv. Mater.*, 2021, **33**, e2008785.

[33] D. G. Billing and A. Lemmerer, Bis [(S)—-phenethylammonium] tribromoplumbate (II). *Acta Crystallogr. Sect. Sect. E: Struct. Rep. Online*, 2003, **59**, m381–m383.

[34] M. Pols, G. Brocks, S. Calero and S. Tao, Temperature-Dependent Chirality in Halide Perovskites. *J. Phys. Chem. Lett.*, 2024, **15**, 8057–8064.

[35] H. Kim, W. Choi, Y. J. Kim, J. Kim, J. Ahn, I. Song, M. Kwak, J. Kim, J. Park, D. Yoo, J. Park, S. K. Kwak and J. H. Oh, Giant chiral amplification of chiral 2D perovskites via dynamic crystal reconstruction. *Sci. Adv.*, 2024, **10**, eado5942.

[36] H. Zhu, K. Miyata, Y. Fu, J. Wang, P. P. Joshi, D. Niesner, K. W. Williams, S. Jin and X.-Y. Zhu, Screening in crystalline liquids protects energetic carriers in hybrid perovskites. *Science*, 2016, **353**, 1409–1413.

[37] A. D. Wright, C. Verdi, R. L. Milot, G. E. Eperon, M. A. Pérez-Osorio, H. J. Snaith, F. Giustino, M. B. Johnston and L. M. Herz, Electron-phonon coupling in hybrid lead halide perovskites. *Nat. Commun.*, 2016, **7**, 11755.

[38] G. R. Berdiyorov, A. Kachmar, F. El-Mellouhi, M. A. Carignano and M. E. Madjet, Role of Cations on the Electronic Transport and Optical Properties of Lead-Iodide Perovskites. *J. Phys. Chem. C*, 2016, **120**, 16259–16270.

[39] L. M. Herz, Charge-Carrier Mobilities in Metal Halide Perovskites: Fundamental Mechanisms and Limits. *Acs Energy Lett.*, 2017, **2**, 1539–1548.

[40] M. Park, A. J. Neukirch, S. E. Reyes-Lillo, M. Lai, S. R. Ellis, D. Dietze, J. B. Neaton, P. Yang, S. Tretiak and R. A. Mathies, Excited-state vibrational dynamics toward the polaron in methylammonium lead iodide perovskite. *Nat. Commun.*, 2018, **9**, 2525.

[41] J. Ibaceta-Jaña, R. Muydinov, P. Rosado, H. Mirhosseini, M. Chugh, O. Nazarenko, D. N. Dirin, D. Heinrich, M. R. Wagner, T. D. Kühne, B. Szyszka, M. V. Kovalenko and A. Hoffmann, Vibrational dynamics in lead halide hybrid perovskites investigated by Raman spectroscopy. *Physical Chemistry Chemical Physics*, 2020, **22**, 5604–5614.

[42] N. P. Gallop, O. Selig, G. Giubertoni, H. J. Bakker, Y. L. A. Rezus, J. M. Frost, T. L. C. Jansen, R. Lovrincic and A. A. Bakulin, Rotational Cation Dynamics in Metal Halide Perovskites: Effect on Phonons and Material Properties. *J. Phys. Chem. Lett.*, 2018, **9**, 5987–5997.

[43] K. Druzbicki, P. Gila-Herranz, P. Marin-Villa, M. Gaboardi, J. Armstrong and F. Fernandez-Alonso, Cation Dynamics as Structure Explorer in Hybrid PerovskitesThe Case of $MAPbI_3$. *Cryst. Growth Des.*, 2024, **24**, 391–404.

[44] P. Calado, A. M. Telford, D. Bryant, X. Li, J. Nelson, B. C. O'Regan and P. R. F. Barnes, Evidence for ion migration in hybrid perovskite solar cells with minimal hysteresis. *Nat. Commun.*, 2016, **7**, 13831.

[45] Y. Yuan and J. Huang, Ion Migration in Organometal Trihalide Perovskite and Its Impact on Photovoltaic Efficiency and Stability. *Acc. Chem. Res.*, 2016, **49**, 286–293.

[46] D. Weber, $CH_3NH_3PbX_3$, ein Pb(II)-System mit kubischer Perowskitstruktur / $CH_3NH_3PbX_3$, a Pb(II)-System with Cubic Perovskite Structure. *Z. Naturforsch.*, 1978, **33**, 1443–1445.

[47] J. M. Frost, K. T. Butler, F. Brivio, C. H. Hendon, M. van Schilfgaarde and A. Walsh, Atomistic origins of high-performance in hybrid halide perovskite solar cells. *Nano Lett.*, 2014, **14**, 2584–90.

[48] D. A. Egger, A. M. Rappe and L. Kronik, Hybrid Organic–Inorganic Perovskites on the Move. *Acc. Chem. Res.*, 2016, **49**, 573–581.

[49] V. Carpenella, C. Fasolato, D. Di Girolamo, J. Barichello, F. Matteocci, C. Petrillo, D. Dini and A. Nucara, Signatures of Polaron Dynamics in Photoexcited $MAPbBr_3$ by Infrared Spectroscopy. *J. Phys. Chem. C*, 2023, **127**, 22097–22104.

[50] V. K. Sharma, R. Mukhopadhyay, A. Mohanty, M. Tyagi, J. P. Embs and D. D. Sarma, Contrasting Behaviors of FA and MA Cations in $APbBr_3$. *J. Phys. Chem. Lett.*, 2020, **11**, 9669–9679.

[51] I. P. Swainson, C. Stock, S. F. Parker, L. Van Eijck, M. Russina and J. W. Taylor, From soft harmonic phonons to fast relaxational dynamics in $CH_3NH_3PbBr_3$. *Phys. Rev. B*, 2015, **92**, 100303.

[52] K. L. Brown, S. F. Parker, I. R. García, S. Mukhopadhyay, V. G. Sakai and C. Stock, Molecular orientational melting within a lead-halide octahedron framework: The order-disorder transition in $CH_3NH_3PbBr_3$. *Phys. Rev. B*, 2017, **96**, 174111.

[53] B. Li, Y. Kawakita, Y. Liu, M. Wang, M. Matsuura, K. Shibata, S. Ohira-Kawamura, T. Yamada, S. Lin, K. Nakajima and S. F. Liu, Polar rotor scattering as atomic-level origin of low mobility and thermal conductivity of perovskite $CH_3NH_3PbI_3$. *Nat. Commun.*, 2017, **8**, 16086.

[54] J. Li, M. Bouchard, P. Reiss, D. Aldakov, S. Pouget, R. Demadrille, C. Aumaitre, B. Frick, D. Djurado, M. Rossi and P. Rinke, Activation Energy of Organic Cation Rotation in $CH_3NH_3PbI_3$ and $CD_3NH_3Pb_3$: Quasi-Elastic Neutron Scattering Measurements and First-Principles Analysis Including Nuclear Quantum Effects. *J. Phys. Chem. Lett.*, 2018, **9**, 3969–3977.

[55] G. Schuck, F. Lehmann, J. Ollivier, H. Mutka and S. Schorr, Influence of Chloride Substitution on the Rotational Dynamics of Methylammonium in $MAPbI_{3-x}Cl_x$ Perovskites. *J. Phys. Chem. C*, 2019, **123**, 11436–11446.

[56] M. Songvilay, Z. Wang, V. G. Sakai, T. Guidi, M. Bari, Z. G. Ye, G. Xu, K. L. Brown, P. M. Gehring and C. Stock, Decoupled molecular and inorganic framework dynamics in $CH_3NH_3PbCl_3$. *Phys. Rev. Mater.*, 2019, **3**, 125406.

[57] A. A. Koegel, E. M. Mozur, I. W. H. Oswald, N. H. Jalarvo, T. R. Prisk, M. Tyagi and J. R. Neilson, Correlating Broadband Photoluminescence with Structural Dynamics in Layered Hybrid Halide Perovskites. *J. Am. Chem. Soc.*, 2022, **144**, 1313–1322.

[58] A. A. Koegel, I. W. H. Oswald, C. Rivera, S. L. Miller, M. J. Fallon, T. R. Prisk, C. M. Brown and J. R. Neilson, Influence of Inorganic Layer Thickness on Methylammonium Dynamics in Hybrid Perovskite Derivatives. *Chem. Mater.*, 2022, **34**, 8316–8323.

[59] E. M. Mozur, M. A. Hope, J. C. Trowbridge, D. M. Halat, L. L. Daemen, A. E. Maughan, T. R. Prisk, C. P. Grey and J. R. Neilson, Cesium Substitution Disrupts Concerted Cation Dynamics in Formamidinium Hybrid Perovskites. *Chem. Mater.*, 2020, **32**, 6266–6277.

[60] K. Druzbicki, R. Lavén, J. Armstrong, L. Malavasi, F. Fernandez-Alonso and M. Karlsson, Cation Dynamics and Structural Stabilization in Formamidinium Lead Iodide Perovskites. *J. Phys. Chem. Lett.*, 2021, **12**, 3503–3508.

[61] D. J. Kubicki, S. D. Stranks, C. P. Grey and L. Emsley, NMR spectroscopy probes microstructure, dynamics and doping of metal halide perovskites. *Nat. Rev. Chem.*, 2021, **5**, 624–645.

[62] G. M. Bernard, R. E. Wasylishen, C. I. Ratcliffe, V. Terskikh, Q. Wu, J. M. Buriak and T. Hauger, Methylammonium Cation Dynamics in Methylammonium Lead Halide Perovskites: A Solid-State NMR Perspective. *J. Phys. Chem. A*, 2018, **122**, 1560–1573.

[63] D. J. Kubicki, D. Prochowicz, A. Hofstetter, P. Pechy, S. M. Zakeeruddin, M. Gratzel and L. Emsley, Cation Dynamics in Mixed-Cation $MA_xFA_{1-x}PbI_3$ Hybrid Perovskites from Solid-State NMR. *J. Am. Chem. Soc.*, 2017, **139**, 10055–10061.

[64] A. A. Bakulin, O. Selig, H. J. Bakker, Y. L. Rezus, C. Muller, T. Glaser, R. Lovrincic, Z. Sun, Z. Chen, A. Walsh, J. M. Frost and T. L. Jansen, Real-Time Observation of Organic Cation Reorientation in Methylammonium Lead Iodide Perovskites. *J. Phys. Chem. Lett.*, 2015, **6**, 3663–9.

[65] O. Selig, A. Sadhanala, C. Muller, R. Lovrincic, Z. Chen, Y. L. Rezus, J. M. Frost, T. L. Jansen and A. A. Bakulin, Organic Cation Rotation and Immobilization in Pure and Mixed Methylammonium Lead-Halide Perovskites. *J. Am. Chem. Soc.*, 2017, **139**, 4068–4074.

[66] A. Mattoni, A. Filippetti, M. I. Saba and P. Delugas, Methylammonium Rotational Dynamics in Lead Halide Perovskite by Classical Molecular Dynamics: The Role of Temperature. *J. Phys. Chem. C*, 2015, **119**, 17421–17428.

[67] A. Mattoni, A. Filippetti and C. Caddeo, Modeling hybrid perovskites by molecular dynamics. *J. Phys.: Condens. Matter*, 2017, **29**, 043001.

[68] E. Mosconi, C. Quarti, T. Ivanovska, G. Ruani and F. De Angelis, Structural and electronic properties of organo-halide lead perovskites: a combined IR-spectroscopy and ab initio molecular dynamics investigation. *Phys. Chem. Chem. Phys.*, 2014, **16**, 16137–44.

[69] D. Ghosh, D. Acharya, L. Pedesseau, C. Katan, J. Even, S. Tretiak and A. J. Neukirch, Charge carrier dynamics in two-dimensional hybrid perovskites: Dion–Jacobson vs. Ruddlesden–Popper phases. *J Mater Chem A*, 2020, **8**, 22009–22022.

[70] A. Mishra, M. A. Hope, M. Gratzel and L. Emsley, A Complete Picture of Cation Dynamics in Hybrid Perovskite Materials from Solid-State NMR Spectroscopy. *J. Am. Chem. Soc.*, 2023, **145**, 978–990.

[71] X. Hu, D. Zhang, T. Chen, A. Z. Chen, E. N. Holmgren, Q. Zhang, D. M. Pajerowski, M. Yoon, G. Xu, J. J. Choi and S. H. Lee, Crystal structures and rotational dynamics of a two-dimensional metal halide perovskite $(OA)_2PbI_4$. *J. Phys. Chem.*, 2020, **152**, 014703.

[72] S. Shao, J. Liu, G. Portale, H.-H. Fang, G. R. Blake, G. H. ten Brink, L. J. A. Koster and M. A. Loi, Highly Reproducible Sn-Based Hybrid Perovskite Solar Cells with 9.

[73] A. Singh, K. M. Boopathi, A. Mohapatra, Y. F. Chen, G. Li and C. W. Chu, Photovoltaic Performance of Vapor-Assisted Solution-Processed Layer Polymorph of $Cs_3Sb_2I_9$. *ACS Appl. Mater. Interfaces*, 2018, **10**, 2566–2573.

[74] T. Zhu, Y. Yang and X. Gong, Recent Advancements and Challenges for Low-Toxicity Perovskite Materials. *ACS Appl. Mater. Interfaces*, 2020, **12**, 26776–26811.

[75] T. Krishnamoorthy, H. Ding, C. Yan, W. L. Leong, T. Baikie, Z. Zhang, M. Sherburne, S. Li, M. Asta, N. Mathews and S. G. Mhaisalkar, Lead-free germanium iodide perovskite materials for photovoltaic applications. *J Mater Chem A*, 2015, **3**, 23829–23832.

[76] A. Babayigit, D. Duy Thanh, A. Ethirajan, J. Manca, M. Muller, H.-G. Boyen and B. Conings, Assessing the toxicity of Pb- and Sn-based perovskite solar cells in model organism Danio rerio. *Sci. Rep.*, 2016, **6**, 18721.

[77] J. P. Cao and F. Yan, Recent progress in tin-based perovskite solar cells. *Energy  Environmental Science*, 2021, **14**, 1286–1325.

[78] E. C. Schueller, G. Laurita, D. H. Fabini, C. C. Stoumpos, M. G. Kanatzidis and R. Seshadri, Crystal Structure Evolution and Notable Thermal Expansion in Hybrid Perovskites Formamidinium Tin Iodide and Formamidinium Lead Bromide. *lnorg. Chem.*, 2018, **57**, 695–701.

[79] A. E. Maughan, A. M. Ganose, A. M. Candia, J. T. Granger, D. O. Scanlon and J. R. Neilson, Anharmonicity and Octahedral Tilting in Hybrid Vacancy-Ordered Double Perovskites. *Chem. Mater.*, 2018, **30**, 472–483.

[80] W. D. Cai, C. Y. Kuang, T. J. Liu, Y. Q. Shang, J. Zhang, J. J. Qin and F. Gao, Multicolor light emission in manganese-based metal halide composites. *Applied Physics Reviews*, 2022, **9**, 041409.

[81] E. Rutherford, Bakerian Lecture: Nuclear constitution of atoms. *Proceedings of the Royal Society of London Series a-Containing Papers of a Mathematical and Physical Character*, 1920, **97**, 374–400.

[82] W. D. Harkins, XXXIX. The constitution and stability of atom nuclei. (A contribution to the subject of inorganic evolution.). *The London, Edinburgh, and Dublin Philosophical Magazine and Journal of Science*, 1921, **42**, 305–339.

[83] J. Chadwick, Possible existence of a neutron. *Nature*, 1932, **129**, 312–312.

[84] R. C. Greenwood and R. E. Chrien, Neutron mass: Measurement of the H1(n,) H2 ray and revised values for selected neutron binding energies. *Phys. Rev. C*, 1980, **21**, 498–502.

[85] F. M. Gonzalez, E. M. Fries, C. Cude-Woods, T. Bailey, M. Blatnik, L. J. Broussard, N. B. Callahan, J. H. Choi, S. M. Clayton, S. A. Currie, M. Dawid, E. B. Dees, B. W. Filippone, W. Fox, P. Geltenbort, E. George, L. Hayen, K. P. Hickerson, M. A. Hoffbauer, K. Hoffman, A. T. Holley, T. M. Ito, A. Komives, C. Y. Liu, M. Makela, C. L. Morris, R. Musedinovic, C. O'Shaughnessy, R. W. Pattie, J. Ramsey, D. J. Salvat, A. Saunders, E. I. Sharapov, S. Slutsky, V. Su, X. Sun, C. Swank, Z. Tang, W. Uhrich, J. Vanderwerp, P. Walstrom, Z. Wang, W. Wei, A. R. Young and U. C. Collaboration, Improved Neutron Lifetime Measurement with UCNtau. *Phys. Rev. Lett.*, 2021, **127**, 162501.

[86] G. L. Greene, N. F. Ramsey, W. Mampe, J. M. Pendlebury, K. Smith, W. B. Dress, P. D. Miller and P. Perrin, Measurement of the Neutron Magnetic-Moment. *Phys. Rev. D*, 1979, **20**, 2139–2153.

[87] R. Hempelmann, *Quasielastic Neutron Scattering and Solid State Diffusion*, Oxford University Press, 2000.

[88] P. Luger, *Modern X-Ray Analysis on Single Crystals*, De Gruyter, Berlin, Boston, 2014.

[89] D. A. Neumann, Neutron scattering and hydrogenous materials. *Mater. Today*, 2006, **9**, 34–41.

[90] W. E. Fischer, SINQ — The spallation neutron source, a new research facility at PSI. *Physica B*, 1997, **234-236**, 1202–1208.

[91] S. Janssen, J. Mesot, L. Holitzner, A. Furrer and R. Hempelmann, FOCUS: A hybrid TOF-spectrometer at SINQ. *Physica B*, 1997, **234**, 1174–1176.

[92] J. Mesota, S. Janssen, L. Holitzner and R. Hempelmann, FOCUS: Project of a space and time focussing time-of-flight spectrometer for cold neutrons at the Spallation Source SINQ of the Paul Scherrer Institute. *J. Neutron Res.*, 1996, **3**, 293–310.

[93] `https://www.psi.ch/en/sinq/focus/description`.

[94] R. Lavén, Dynamical properties of metal halide and oxyhydride perovskites. *Thesis*, 2023.

[95] R. Shannon, Revised effective ionic radii and systematic studies of interatomic distances in halides and chalcogenides. *Acta Crystallogr. Sect. A*, 1976, **32**, 751–767.

[96] A. Pisanu, A. Mahata, E. Mosconi, M. Patrini, P. Quadrelli, C. Milanese, F. De Angelis and L. Malavasi, Exploring the Limits of Three-Dimensional Perovskites: The Case of $FAPb_{1-x}SnxBr_3$. *Acs Energy Lett.*, 2018, **3**, 1353–1359.

[97] D. J. Kubicki, D. Prochowicz, E. Salager, A. Rakhmatullin, C. P. Grey, L. Emsley and S. D. Stranks, Local Structure and Dynamics in Methylammonium, Formamidinium, and Cesium Tin(II) Mixed-Halide Perovskites from 119Sn Solid-State NMR. *J. Am. Chem. Soc.*, 2020, **142**, 7813–7826.

[98] C. Yu, Y. Kawakita, T. Kikuchi, M. Kofu, T. Honda, Z. Zhang, Z. Zhang, Y. Liu, S. F. Liu and B. Li, Atomic Structure and Dynamics of Organic–Inorganic Hybrid Perovskite Formamidinium Lead Iodide. *J. Phys. Chem. Lett.*, 2024, **15**, 329–338.

[99] W. D. Cai, J. J. Qin, T. Q. Pang, X. Y. Cai, R. X. Jia and F. Gao, Chirality Induced Crystal Structural Difference in Metal Halide Composites. *Advanced Optical Materials*, 2022, **10**, 16.

[100] M. T. Weller, O. J. Weber, J. M. Frost and A. Walsh, Cubic Perovskite Structure of Black Formamidinium Lead Iodide, $-[HC(NH_2)_2]PbI_3$, at 298 K. *J. Phys. Chem. Lett.*, 2015, **6**, 3209–3212.

[101] R. Laref, F. Massuyeau and R. Gautier, Role of Hydrogen Bonding on the Design of New Hybrid Perovskites Unraveled by Machine Learning. *Small*, 2024, **20**, 5.

[102] P. R. Varadwaj, A. Varadwaj, H. M. Marques and K. Yamashita, Significance of hydrogen bonding and other noncovalent interactions in determining octahedral tilting in the $CH_3$ $NH_3$ $PbI_3$ hybrid organic-inorganic halide perovskite solar cell semiconductor. *Sci. Rep.*, 2019, **9**, 50.

[103] A. Garrote-Márquez, L. Lodeiro, R. Suresh, N. C. Hernández, R. Grau-Crespo and E. Menéndez-Proupin, Hydrogen Bonds in Lead Halide Perovskites: Insights from Molecular Dynamics. *J. Phys. Chem. C*, 2023, **127**, 15901–15910.

[104] Y. Natanzon, A. Azulay and Y. Amouyal, Evaluation of Polaron Transport in Solids from First-principles. *Isr. J. Chem.*, 2020, **60**, 768–786.

[105] D. Meggiolaro, F. Ambrosio, E. Mosconi, A. Mahata and F. De Angelis, Polarons in Metal Halide Perovskites. *Adv. Energy Mater.*, 2020, **10**, 13.

[106] K. T. Munson, G. S. Doucette, E. R. Kennehan, J. R. Swartzfager and J. B. Asbury, Vibrational Probe of the Structural Origins of Slow Recombination in Halide Perovskites (vol 123, pg 7061, 2019). *J. Phys. Chem. C*, 2019, **123**, 21822–21822.

[107] N. Aihemaiti, Z. Li and S. Peng, Perspective on High-Resolution Characterizations of Polarons in Halide Perovskites. *Chem. Mater.*, 2024.

[108] A. Koda, H. Okabe, M. Hiraishi, R. Kadono, K. A. Dagnall, J. J. Choi and S. H. Lee, Organic molecular dynamics and charge-carrier lifetime in lead iodide perovskite $MAPbI_3$. *Proc. Natl. Acad. Sci. U.S.A.*, 2022, **119**, 119 (4) e2115812119.

[109] H.-G. Duan, V. Tiwari, A. Jha, G. R. Berdiyorov, A. Akimov, O. Vendrell, P. K. Nayak, H. J. Snaith, M. Thorwart, Z. Li, M. E. Madjet and R. J. D. Miller, Photoinduced Vibrations Drive Ultrafast Structural Distortion in Lead Halide Perovskite. *J. Am. Chem. Soc.*, 2020, **142**, 16569–16578.

[110] A. J. Neukirch, W. Nie, J.-C. Blancon, K. Appavoo, H. Tsai, M. Y. Sfeir, C. Katan, L. Pedesseau, J. Even, J. J. Crochet, G. Gupta, A. D. Mohite and S. Tretiak, Polaron Stabilization by Cooperative Lattice Distortion and Cation Rotations in Hybrid Perovskite Materials. *Nano Lett.*, 2016, **16**, 3809–3816.

[111] J. Gong, M. Yang, X. Ma, R. D. Schaller, G. Liu, L. Kong, Y. Yang, M. C. Beard, M. Lesslie, Y. Dai, B. Huang, K. Zhu and T. Xu, Electron-Rotor Interaction in Organic-Inorganic Lead Iodide Perovskites Discovered by Isotope Effects. *J. Phys. Chem. Lett.*, 2016, **7**, 2879–87.

[112] G. Kieslich, J. M. Skelton, J. Armstrong, Y. Wu, F. X. Wei, K. L. Svane, A. Walsh and K. T. Butler, Hydrogen Bonding versus Entropy: Revealing the Underlying Thermodynamics of the Hybrid Organic-Inorganic Perovskite $[CH_3NH_3]PbBr_3$. *Chem. Mater.*, 2018, **30**, 8782–8788.

Appendix A

# Working principles of perovskite devices

The brief structures and energy diagrams of common MHP devices are shown in Figure A.1. The general working principle of a perovskite solar cell is that the electrons in the valence band absorb sunlight and transition to the conduction band, passing through the electron transport layer collected by the electrode. The original vacancies of the excited electrons can be regarded as positive charges, called holes, passing through the hole transport layer and

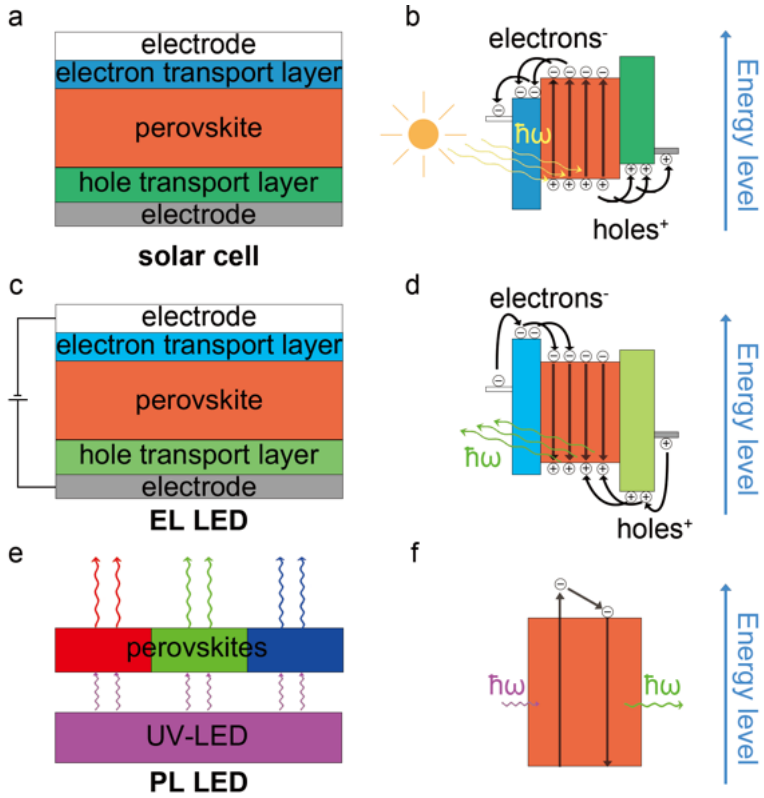


Figure A.1: Schematic of the MHPs devices and energy diagrams including (a) and (b): perovskite solar cell, (c) and (d): electroluminescent (EL) perovskite LED, and (e) and (f): photoluminescent (PL) perovskite LED

being collected by the electrode, thereby converting light energy into electrical energy [Figure A.1(b)]. The working principle of EL perovskite LED is the opposite process to that of a solar cell. Electric energy is input through the electrode from an external voltage source, and electrons are transported to the perovskite layer through the electron transport layer. In the perovskite layer, electrons and holes can have radiative recombination to release photons [Figure A.1(d)]. The working principle of perovskite PL LED is to use a shorter wavelength (ultraviolet or blue light) light source to excite the valence band electrons in perovskites to the conduction band, and then release photons through radiation recombination. This is mainly used to obtain an adjustable emission peak to fabricate the display pixels through the primary colors or to obtain a broader emission peak to obtain white light emission for lighting [Figure A.1(f)]. It is important to point out that the real device structure is usually more complex and can have more layers such as a hole-blocking layer to have better device efficiency and performance.

Appendix B

# Several details of neutron scattering theory

## B.1 Cross section and scattering length

The incident neutron can be generally described as a plane wave[A.1]:

$$\psi_i(\mathbf{R}) = \frac{1}{\sqrt{Y}} e^{ik\cdot\mathbf{R}} \tag{B.1}$$

where $Y$ represents a normalization constant, and $\mathbf{R}$ is the position operator. The scattered neutron wavefront can be described as a spherical wave[A.1]:

$$\psi_f(\mathbf{R}) = \psi_i(\mathbf{R}_j) \frac{-b_j}{|\mathbf{R}-\mathbf{R}_j|} e^{ik_f|\mathbf{R}-\mathbf{R}_j|} \tag{B.2}$$

where $\mathbf{R}_j$ is the position operator of nuclei $j$ and $|\mathbf{R}-\mathbf{R}_j| \gg b_j$, where $b_j$ is the scattering length which can be considered as the scattering ability/character from the nuclei and it can be found from the wave expansion's first term[A.2]:

$$\lim_{k\to 0} k\cot\delta(k) = -\frac{1}{b_j} \tag{B.3}$$

where $\delta(k)$ is the phase shift of the outgoing spherical wave. The total inelastic scattering cross section can be found[A.1]:

$$\sigma = \int_{4\pi}\int_{-\infty}^{\infty} \frac{d^2\sigma}{d\Omega dE_f} dE_f d\Omega \tag{B.4}$$

$$\frac{d\sigma}{d\Omega} = \int_{-\infty}^{\infty} \frac{d^2\sigma}{d\Omega dE_f} dE_f \tag{B.5}$$

## B.2 Correlation functions

Now we consider the situation of scattering interference from multiple nuclei. Considering the scattering as the perturbation $\hat{V}$ and following the Fermi

pseudopotential for nuclear scattering we can get [A.3,A.4]:

$$\hat{V} = \frac{2\pi\hbar^2}{m_n} \sum_j P_j b_j \delta(\mathbf{R} - \mathbf{R}_j) \tag{B.6}$$

where $P_j$ is the statistical weight of the thermal occupancy [A.4]:

$$P_j = \frac{e^{-E_j/k_\mathrm{B}T}}{\sum_n e^{-E_n/k_\mathrm{B}T}} \tag{B.7}$$

and $m_\mathrm{n}$ is the neutron mass, $R_j$ is the operator for $j_\mathrm{th}$ nucleus position. The initial and final sample states are denoted as $|\lambda_\mathrm{i}\rangle$ and $|\lambda_\mathrm{f}\rangle$, The partial differential cross section for scattering from $|\lambda_\mathrm{i}, k_\mathrm{i}\rangle$ to $|\lambda_\mathrm{f}, k_\mathrm{f}\rangle\rangle$ through the Fermi Golden Rule [A.4,A.5]:

$$\begin{aligned} \left.\frac{d^2\sigma}{d\Omega dE_f}\right|_{\lambda_\mathrm{i}\to\lambda_\mathrm{f}} &= \frac{k_\mathrm{f}}{k_\mathrm{i}} (\frac{m_\mathrm{n}}{2\pi\hbar^2})^2 |\langle\lambda_\mathrm{i} k_\mathrm{i}|\hat{V}|\lambda_\mathrm{f} k_\mathrm{f}\rangle|^2 \delta(E_{\lambda_i} - E_{\lambda_f} + \hbar\omega) \\ &= \frac{k_\mathrm{f}}{k_\mathrm{i}} \sum_{j,j'} \frac{b_j b_{j'}}{2\pi\hbar} \int_{-\infty}^{\infty} \langle e^{-i\mathbf{Q}\cdot\mathbf{R}_j(0)} e^{i\mathbf{Q}\cdot\mathbf{R}_{j'}(t)}\rangle e^{-i\omega t} dt \end{aligned} \tag{B.8}$$

where $j'$ represents the different nuclei which can have different cross-sections when we consider the coherent scattering. We denote thermal averaging by the notation [A.4]:

$$\langle A\rangle \equiv \sum_i p_i \langle\lambda_i|A|\lambda_i\rangle \tag{B.9}$$

where $p_i$ is the Boltzmann probability for the individual states.

The dynamical correlation function as known as the scattering function $S(\mathbf{Q}, \omega)$ is defined as [A.4]:

$$S(\mathbf{Q},\omega) = \sum_{j,j'} \frac{b_j b_{j'}}{2\pi\hbar N} \int_{-\infty}^{\infty} \langle e^{-i\mathbf{Q}\cdot\mathbf{R}_j(0)} e^{i\mathbf{Q}\cdot\mathbf{R}_{j'}(t)}\rangle e^{-i\omega t} dt \tag{B.10}$$

$$\frac{d^2\sigma}{d\Omega dE_f} = \frac{k_\mathrm{f}}{k_\mathrm{i}} N S(\mathbf{Q},\omega) \tag{B.11}$$

where N represents the number of nuclei. From the Fourier transform of the intermediate function over time leads to [A.4]:

$$I(\mathbf{Q},t) = \frac{1}{N} \sum_{j,j'} b_j b_{j'} \langle e^{-i\mathbf{Q}\cdot\mathbf{R}_j(0)} e^{i\mathbf{Q}\cdot\mathbf{R}_{j'}(t)}\rangle \tag{B.12}$$

Applying another Fourier transformation over $Q$ will transform the intermediate correlation function into the space-time correlation function [A.4]:

$$G(\mathbf{R},t) = \frac{1}{(2\pi)^3} \int I(\mathbf{Q},t) e^{-i\mathbf{Q}\cdot\mathbf{R}} d\mathbf{Q} \tag{B.13}$$

## B.3 Coherent and incoherent scattering

A sample contains a large amount of different nuclei and isotopes with different cross sections and spin states, which means that when the neutron is scattered by the sample, it may be affected by different nuclei and cause interference. Each nucleus cross section can also be different in time due to the variations of nuclear spin. To explore these problems, assuming that the scattering length of a nucleus in the sample is divided into the time and ensemble mean value $\langle b_j \rangle$ and the local and temporal deviation value $\delta b_j$ [A.1]:

$$b_j = \langle b_j \rangle + \delta b_j \tag{B.14}$$

where $\langle \delta b_j \rangle = 0$ can be found from the definition. From eq. 3.2, eq. B.2 and eq. B.14, for whole nucleus in the system:

$$\begin{aligned} \langle \frac{d\sigma}{d\Omega} \rangle &= \sum_j \langle (\delta b_j)^2 \rangle + |\sum_j \langle b_j \rangle e^{i\mathbf{Q}\mathbf{R}_j}|^2 \\ &= \frac{d\sigma_{\text{inc}}}{d\Omega} + \frac{d\sigma_{\text{coh}}}{d\Omega} \end{aligned} \tag{B.15}$$

The incoherent quasielastic neutron scattering, which is the main type of scattering involved in this thesis, is caused by atomic self-diffusion. Following the eq. B.8 and B.15, the incoherent part of the double differential of the cross-section can be derived:

$$\left. \frac{d^2\sigma_{\text{inc}}}{d\Omega dE_f} \right|_{\lambda_{\text{i}} \to \lambda_{\text{f}}} = \frac{k_{\text{f}}}{k_{\text{i}}} \sum_j \frac{\langle (\delta b_j)^2 \rangle}{2\pi\hbar} \int_{-\infty}^{\infty} \langle e^{-i\mathbf{Q}\cdot\mathbf{R}_j(0)} e^{i\mathbf{Q}\cdot\mathbf{R}_{j'}(t)} \rangle e^{-i\omega t} dt \tag{B.16}$$

## B.4 Jump diffusion models

The jump diffusion model can be described through the probability $p(R_a, t)$ of finding the particle at position $r_a$ at time $t$ with expected residence time $\tau_a$ within total $N$ possible sites, and $\tau_{a,b}^{-1}$ is the jump probability from $R_a$ to $R_b$, then we have:

$$\tau_a^{-1} = \sum_{b=1, b\neq a}^{N} \tau_{a,b}^{-1} \tag{B.17}$$

$$\frac{d}{dt} p(\mathbf{R}_a, t) = \sum_{b=1, b\neq a}^{N} p(\mathbf{R}_b, t) \tau_{b,a}^{-1} - p(\mathbf{R}_a, t) \sum_{b=1, b\neq a}^{N} \tau_{a,b}^{-1} \tag{B.18}$$

Then we can obtain the probability $p(\mathbf{R}_b, t; \mathbf{R}_a, 0)$ which represents the probability the particle at position $\mathbf{R}_a$ at $t = 0$ can be found at position $\mathbf{R}_b$ at $t$ by setting the initial condition $p(\mathbf{R}_a, 0) = 1$ to solve the differential eq. B.18.

we can obtain the incoherent intermediate scattering function $I(\mathbf{Q},t)$ (trans-

fer from the general form eq. B.12):

$$I(\mathbf{Q},t) = \sum_{a=1}^{N} p(\mathbf{R}_a,0)\langle e^{i\mathbf{Q}[\mathbf{R}_a(t)-\mathbf{R}_a(0)]}\rangle \tag{B.19}$$

$$= \sum_{a=1}^{N} p(\mathbf{R}_a,0)[\sum_{b=1}^{N} p(\mathbf{R}_b,t;\mathbf{R}_a,0)e^{i\mathbf{Q}(\mathbf{R}_b-\mathbf{R}_a)}] \tag{B.20}$$

Subsequently, by setting the equilibrium conditions of initial distribution ($t = 0$):

$$p(\mathbf{R}_a,0) = \tau_a / \sum_{n=1}^{N} \tau_n = P_a \tag{B.21}$$

we can obtain the $S(\mathbf{Q},\omega)$ through the Fourier transform of $I(\mathbf{Q},t)$:

$$S(\mathbf{Q},E) = \frac{1}{2\pi}\int I(\mathbf{Q},t)e^{-iEt}dt \tag{B.22}$$

$$= \sum_{a=1}^{N} P_a A_{0\_a}(\mathbf{Q})\delta(\mathbf{Q},E) + \sum_{a=1}^{N} P_a \sum_{b\neq a}^{N} p(\mathbf{R}_b,t;\mathbf{R}_a,0)A_{a,b}(\mathbf{Q})\mathcal{L}_{a,b}(\mathbf{Q},E) \tag{B.23}$$

The structure factors for several common models are presented below:

**2-site jump diffusion**

The 2-site jump diffusion can be obtained by considering the particle jump between two sites with mean residence time $\tau_1$ and $\tau_2$ and jump distance $d = |\mathbf{R}_1 - \mathbf{R}_2|$, see Figure 3.5(a).[A.4] From eq.3.10:

$$S(Q,E) = A_0(Q)\delta(E) + A_1(Q)\frac{1}{\pi}\frac{\hbar(\tau_1^{-1}+\tau_2^{-1})}{[\hbar(\tau_1^{-1}+\tau_2^{-1}]^2 + E^2} \tag{B.24}$$

$$A_0(Q) = P_1^2 + P_2^2 + 2P_1P_2j_0(Qd) \tag{B.25}$$

$$A_1(Q) = 2P_1P_2[1 - j_0(Qd)] \tag{B.26}$$

**Diffusion on a circle**

In this model, it is supposed that the particle can only directly go to the nearest two sites on the circle, for instance in Figure 3.5(b), when the particle is on the site $\mathbf{R}_i$ the next jump of it can only jump to $\mathbf{R}_{i-1}$ or $\mathbf{R}_{i+1}$. In other words, $\tau_{i,j}^{-1} = 0$ when $|i-j|>1$. Considering the equivalent site model, N residence

sites are evenly separated on the circle, from eq. 3.10[A.4,A.6]:

$$S(Q,E) = A_0(Q)\delta(E) + \sum_{i=1}^{N-1} A_i(Q)\frac{1}{\pi}\frac{\hbar/\tau_i}{(\hbar/\tau_i)^2 + E^2} \tag{B.27}$$

$$A_i(Q) = \frac{1}{N}\sum_{n=1}^{N} j_0(Qr_n)cos(\frac{2in\pi}{N}) \tag{B.28}$$

$$r_n = 2r \cdot sin(\frac{n\pi}{N}) \tag{B.29}$$

$$\tau_i^{-1} = 2\tau^{-1}sin^2(\frac{\pi \cdot i}{N}) \tag{B.30}$$

it can be considered as a continuously rotational diffusion when $N \to +\infty$.

### Diffusion on a sphere

As known as the isotropic reorientation, it is similar to the underlying logic of the previous model, an equivalent site model is also considered, but considering the spatial angle, see Figure 3.5(c). The function is as follows[A.4,A.6]:

$$S(Q,E) = A_0(Q)\delta(E) + \sum_{i=1}^{\infty} A_i(Q)\frac{1}{\pi}\frac{\hbar/\tau}{(\hbar/\tau)^2 + E^2} \tag{B.31}$$

$$A_i(Q) = (2i+1)j_i^2(Qr) \tag{B.32}$$

$$\tau_i^{-1} = i(i+1)D_{\mathrm{R}} \tag{B.33}$$

where $r$ is the radius of the sphere, $D_{\mathrm{R}}$ is the rotational diffusion coefficient (in units of radians$^2$/s).

Since there are numerous independent variables $\tau_a$, we cannot provide an analytical solution for the $A_{a,b}(\mathbf{Q})\mathcal{L}_{a,b}(\mathbf{Q},\omega)$. But here is the general solution for elastic incoherent structure factor (EISF) $A_0(\mathbf{Q})$ by setting $t \to \infty$. The equilibrium distribution is obtained when $t \to \infty$, $p(R_b, t; R_a, 0) = P_b$ which is independent of the initial site for the particle.

Thus from eq. B.21, B.20 we can have the $t$ independent term $A_0(\mathbf{Q})$ of $I(\mathbf{Q},t)$:

$$I(\mathbf{Q}, t \to \infty) = \sum_{a=1,b=1}^{N} P_a P_b \cdot \cos[\mathbf{Q}(\mathbf{R}_a - \mathbf{R}_b)] \tag{B.34}$$

$$= A_0(\mathbf{Q}) = \mathrm{EISF} \tag{B.35}$$

By Fourier transformation over time:

$$S(\mathbf{Q}, E \to 0) = A_0(\mathbf{Q})\delta(E) \tag{B.36}$$

in the case of a powder sample:

$$\text{EISF} = \frac{1}{4\pi}\int_0^{2\pi} d\varphi \int_0^{\pi} A_0(\mathbf{Q})\sin(\theta)d\theta \tag{B.37}$$

$$= \sum_{a=1,b=1}^{N} P_a P_b \cdot j_0(Q|\mathbf{R}_a - \mathbf{R}_b|) \tag{B.38}$$

where $j_0(x) = \sin(x)/x$ is the zeroth-order spherical Bessel function.

## B.5 Detailed balance

It is important to introduce the principle of detailed balance which can help us to understand the asymmetry of the $S(\mathbf{Q},E)$ spectrum, especially at relatively low temperatures (Figure 3.3) [A.1]:

$$\begin{aligned} S(-\mathbf{Q},-E)\Big|_{\lambda_f\to\lambda_i} &= S(\mathbf{Q},E)\Big|_{\lambda_i\to\lambda_f} \\ S(-\mathbf{Q},-E) &= \sum_{\lambda_i,\lambda_f} p_{\lambda_f} S(-\mathbf{Q},-E)\Big|_{\lambda_f\to\lambda_i} \\ &= \sum_{\lambda_i,\lambda_f} p_{\lambda_i} \frac{p_{\lambda_f}}{p_{\lambda_i}} S(\mathbf{Q},E)\Big|_{\lambda_i\to\lambda_f} \\ &= e^{-E/(k_B T)} S(\mathbf{Q},E)\Big|_{\lambda_i\to\lambda_f} \end{aligned} \tag{B.39}$$

where $k_\mathrm{B}$ is the Boltzmann constant, $T$ is the temperature. It is a vital step that applies the detail balance before the $S(\mathbf{Q},E)$ spectrum fitting with the QENS signal fitted by the symmetric lorentzians.

## Appendix References

[A.1] K. Lefmann, *Neutron scattering: Theory, instrumentation, and simulation*, 2021.

[A.2] S. Weinberg, *Lectures on Quantum Mechanics*, Cambridge University Press, Cambridge, 2nd edn, 2015.

[A.3] E. Fermi, Sul moto dei neutroni nelle sostanze idrogenate. *Ric. Sci.*, 1936, **7**, 13–52.

[A.4] R. Hempelmann, *Quasielastic Neutron Scattering and Solid State Diffusion*, Oxford University Press, 2000.

[A.5] E. Fermi, *Nuclear physics: a course given by Enrico Fermi at the University of Chicago*, University of Chicago press, 1950.

[A.6] M. Bée, *Quasielastic neutron scattering*, Adam Hilger, United Kingdom, 1988.